The Astrophysical Journal, 894:103 (24pp), 2020 May 10 https://doi.org/10.3847/1538-4357/ab8938

Star Formation Occurs in Dense Gas, but What Does "Dense" Mean?

Neal J. Evans, II[1,2,3], Kee-Tae Kim[2,4], Jingwen Wu[5], Zhang Chao[5], Mark Heyer[6], Tie Liu[2,7], Quang Nguyen-Lu'o'ng[8,9,10], and Jens Kauffmann[11]
[1] Department of Astronomy The University of Texas at Austin 2515 Speedway, Stop C1400 Austin, TX 78712-1205, USA; nje@astro.as.utexas.edu
[2] Korea Astronomy and Space Science Institute 776 Daedeokdae-ro, Yuseong-gu Daejeon, 34055, Republic of Korea
[3] Humanitas College, Global Campus, Kyung Hee University, Yongin-shi 17104, Republic of Korea
[4] University of Science and Technology, Korea (UST), 217 Gajeong-ro, Yuseong-gu, Daejeon 34113, Republic of Korea
[5] National Astronomical Observatories, Chinese Academy of Sciences, 20A Datun Road, Chaoyang District, Beijing, 100012, People's Republic of China
[6] Department of Astronomy University of Massachusetts Amherst, MA 01003, USA
[7] Shanghai Astronomical Observatory, Chinese Academy of Sciences, 80 Nandan Road, Shanghai, 200030, People's Republic of China
[8] McMaster University, 1 James St N, Hamilton, ON, L8P 1A2, Canada
[9] Graduate School of Natural Sciences, Nagoya City University, Mizuho-ku, Nagoya, Aichi 467-8601, Japan
[10] IBM Canada, 120 Bloor Street East, Toronto, ON, M4Y 1B7, Canada
[11] Haystack Observatory MIT 99 Milstone Rd., Westford, MA 01886, USA
Received 2020 February 3; revised 2020 March 25; accepted 2020 April 13; published 2020 May 12

Abstract

We report results of a project to map HCN and HCO^+ $J = 1 \rightarrow 0$ emission toward a sample of molecular clouds in the inner Galaxy, all containing dense clumps that are actively engaged in star formation. We compare these two molecular line tracers with millimeter continuum emission and extinction, as inferred from ^{13}CO, as tracers of dense gas in molecular clouds. The fraction of the line luminosity from each tracer that comes from the dense gas, as measured by $A_V > 8$ mag, varies substantially from cloud to cloud. In all cases, a substantial fraction (in most cases, the majority) of the total luminosity arises in gas below the $A_V > 8$ mag threshold and outside the region of strong millimeter continuum emission. Measurements of L(HCN) toward other galaxies will likely be dominated by such gas at lower surface densities. Substantial, even dominant, contributions to the total line luminosity can arise in gas with densities typical of the cloud as a whole ($n \sim 100\,\mathrm{cm}^{-3}$). Defining the dense clump from the HCN or HCO^+ emission itself, similarly to previous studies, leads to a wide range of clump properties, with some being considerably larger and less dense than in previous studies. HCN and HCO^+ have a similar ability to trace dense gas for the clouds in this sample. For the two clouds with low virial parameters, ^{13}CO is definitely a worse tracer of the dense gas, but for the other four, it is equally good (or bad) at tracing dense gas.

Unified Astronomy Thesaurus concepts: Interstellar medium (847); Molecular clouds (1072); Star formation (1569)

1. Introduction

In pioneering work, Gao & Solomon (2004) showed that the far-infrared luminosities in starburst galaxies follow a very tight, linear correlation with the luminosities of HCN line emission. Wu et al. (2005) showed that this relationship extended to massive, dense clumps in the Milky Way, arguing that the fundamental unit of massive, clustered star formation is such a massive, dense clump. Subsequent studies have defined a "threshold" surface density of $A_V > 8$ mag (about 120 $M_\odot\,\mathrm{pc}^{-2}$) in nearby clouds (Heiderman et al. 2010; Lada et al. 2010, 2012), above which the vast majority of dense cores and YSOs are found. Evans et al. (2014) compared various models of star formation to observations of nearby clouds and found that the mass of dense gas was the best predictor of the star formation rate. Most recently, Vutisalchavakul et al. (2016) showed that a similar result applied to more distant and massive clouds in the Galactic plane, using millimeter continuum emission from the BGPS survey (Ginsburg et al. 2013) to measure the mass of dense gas. Vutisalchavakul et al. (2016) found a substantial dispersion in the star formation rate per mass of dense gas (0.50 dex), but the logarithmic averages of the star formation rate per mass of dense gas were in general agreement for nearby clouds, inner Galaxy clouds, and extragalactic clouds. The dispersion among the averages for these three entities was only 0.19 dex (Figure 11 of Vutisalchavakul et al. 2016), considerably lower than that for total molecular gas probed by CO or ^{13}CO, 0.42 dex (Figure 12 of Vutisalchavakul et al. 2016). The star formation rate per unit mass of dense gas is thus remarkably constant over a huge range of scales and conditions. A recent detailed study of HCN emission toward other galaxies (Jiménez-Donaire et al. 2019) also found a small dispersion (0.22 dex) in the star formation rate per mass of dense gas. After accounting for galaxy-to-galaxy variations, the intra-galaxy dispersion was only 0.12 dex. A smaller dispersion for measurements over an entire galaxy is expected if the dispersion among the clouds within a galaxy is due to variations in the evolutionary state of the molecular cloud (e.g., Kruijssen et al. 2018).

While the tight connection between dense parts of molecular clouds and star formation is clear, we must better define what we mean by "dense". The most direct measure exists for the nearby clouds, where surface density can be determined by extinction maps of background stars. For the Galactic plane clouds, continuum emission by dust or line emission by HCN was used. For other galaxies, HCN emission has been the only tracer of dense gas in general use, although HCO^+ emission has also been explored (Barnes et al. 2011; Privon et al. 2015; Jiménez-Donaire et al. 2019). The extinction maps are strictly sensitive to surface density, while the dust continuum emission is also sensitive to temperature, and the molecular line emission, in addition to surface density and temperature, is sensitive to volume density and abundances. Temperature and molecular abundances can depend on the radiation environment (Pety et al. 2017; Shimajiri et al. 2017). A detailed comparison

of these various tracers of "dense" gas can clarify the situation. In this paper, we will compare maps of HCN, HCO^+, and ^{13}CO $J = 1 \rightarrow 0$ emission to the regions selected as dense by extinction or millimeter-wave continuum emission in a sample of Galactic plane clouds. We refer to all of the molecular lines as "line tracers" and the HCN and HCO^+ lines as "dense line tracers" for convenience, while noting that our purpose is to test the proposition that they trace gas of the density relevant to star formation.

Specifically, we can learn what fraction of the luminosity from the line tracers arises from low-level, extended emission from less dense gas. Stephens et al. (2016) have argued that most of the Galaxy's luminosity of HCN arises from distributed, very sub-thermal, emission rather than from dense gas. Since observations of other galaxies would integrate large areas of low-level emission, their HCN luminosity could be dominated by the same gas that is probed by CO, complicating the connection found by Wu et al. (2005) between dense clumps in the Milky Way and other galaxies. Pioneering work by Helfer & Blitz (1997) showed that HCN emission is very weak compared to CO ($I_{HCN}/I_{CO} = 0.014 \pm 0.020$) averaged over random observations of the Galactic plane. They further showed that maps of HCN $J = 1 \rightarrow 0$ in nearby large molecular clouds were tiny in comparison to the CO maps. This work argues against the idea of Stephens et al. (2016), but improved instrumentation now allows for a much stronger test. Recent work has shown that HCN emission can indeed arise from more extended regions (Pety et al. 2017; Kauffmann et al. 2017; Shimajiri et al. 2017), but the focuses of those studies were all on clouds in the solar neighborhood (out to the distance of the Orion clouds). A recent study extends these results to the M17 cloud Nguyen-Luong et al. (2020).

Maps of the full extent of ^{13}CO emission in inner Galaxy clouds allow us to directly test the contribution of more diffuse molecular gas to the HCN luminosity in a very different environment. The simultaneous observations of HCO^+ provide a direct comparison of these two tracers. One might predict that HCO^+ $J = 1 \rightarrow 0$ traces more widespread gas of lower mean density than does HCN $J = 1 \rightarrow 0$ because the critical density for HCO^+ $J = 1 \rightarrow 0$ at $T_K = 20$ K ($n_{cr} \approx 4.5 \times 10^4$ cm^{-3}) is nearly an order of magnitude less than that for HCN $J = 1 \rightarrow 0$ ($n_{cr} \approx 3.0 \times 10^5$ cm^{-3}; Evans 1999; Shirley 2015). A comparison of these two tracers in a well-defined sample with star formation rates will be useful for evaluating relations seen in extragalactic studies of dense gas. Studies of HCN and HCO^+ have found some evidence of environmental effects in other galaxies, such as the presence of an active galactic nucleus (see, e.g., Privon et al. 2015 for a discussion of this issue). It is important first to understand the relation between these two tracers in more controlled environments. We also evaluate whether ^{13}CO $J = 1 \rightarrow 0$ can trace the relevant gas for star formation; while it has a much lower critical density ($n_{cr} \approx 4.8 \times 10^2$ cm^{-3}), it is easier to observe.

With spectrally resolved maps, we can also assess the balance between gravity and turbulence, most simplistically captured in the virial parameter. One attractive explanation for the low star formation efficiency in molecular clouds is that most clouds are not gravitationally bound; only relatively dense regions within them are bound (Dobbs et al. 2011; Barnes et al. 2016). While studies differ, even the most massive clouds defined by CO emission may be unbound (Nguyen-Luong et al. 2016). By calculating the virial ratio for the structures traced by the different species, we may be able to shed light on this issue.

2. Sample

The target clouds (listed in Table 1) comprise a subset of the Vutisalchavakul et al. (2016) sample, chosen to sample a range of conditions and environments, as well as for suitable size (8–35 pc) and relative lack of confusion. The sample has maps of CO and ^{13}CO from the Five College Radio Astronomy Observatory (FCRAO) and millimeter-wave continuum emission from the Bolocam Galactic Plane Survey (BGPS), obtained at the Caltech Submillimeter Observatory (CSO; Aguirre et al. 2011; Ginsburg et al. 2013), and two measures of the star formation rate, radio continuum, and mid-infrared emission (Vutisalchavakul et al. 2016). The CO and ^{13}CO data were, respectively, taken from the UMass-Stony Brook Survey (Sanders et al. 1986) and the Boston University-FCRAO Galactic Ring Survey (GRS; Jackson et al. 2006). The FWHM beam sizes were 45″ for CO and 46″ for ^{13}CO. The velocity resolutions were 0.65 km s^{-1}, smoothed to 1.0 km s^{-1}, for CO, and 0.21 km s^{-1} for ^{13}CO. The rms noise (in T_A^*) was 0.4 K for CO and 0.13 K for ^{13}CO. The BGPS was obtained with a filter centered at 271.4 GHz and a bandwidth of 46 GHz (avoiding the CO $J = 2 \rightarrow 1$ line) at 33″ effective resolution and rms noise ranging from 11 to 53 mJy beam^{-1} (Aguirre et al. 2011). We use version 2.0 of the BGPS catalog, which has an improved positional accuracy and response to extended structure (Ginsburg et al. 2013). In particular, 95% of the flux was recovered for scales between 33″ and 80″, and emission out to 300″ was partially recovered.

The typical angular extent of BGPS sources is a few arcmin, so we selected clouds with ^{13}CO extents of 10′–20′ to fully sample the "diffuse" gas. The boundaries of the ^{13}CO emission (column 9 of Table 1) were set in order to separate the cloud from the background; they were substantial and varied from cloud to cloud. The procedure was described in Vutisalchavakul et al. (2016), but generally, the threshold was the minimum needed to distinguish the cloud from background/foreground ^{13}CO emission. These thresholds are 5–12 times the rms noise, so the clouds undoubtedly are larger and more massive, but uncertainty in the inner Galaxy limits the region that can be isolated. We favored clouds with at least one BGPS source with a size of at least 3′ so that we can clearly compare the morphology of the HCN/HCO^+ emission and the dust emission. We also favored clouds with larger and stronger BGPS sources. We identified six clouds in the sample of Vutisalchavakul et al. (2016) that meet these criteria. The sample spans a good range of cloud mass ($2.4 \times 10^4\,M_\odot$ to $3.3 \times 10^5\,M_\odot$), dense gas mass (700–$1.3 \times 10^4\,M_\odot$), and star formation rate (23–275 $M_\odot$ Myr^{-1}). While the clouds range in distance from us (3.5–10.4 kpc), all lie between 5.1 and 6.4 kpc from the Galactic center, in the molecular ring.

The distances used by Vutisalchavakul et al. (2016) were mostly taken from Anderson et al. (2014), who used a variety of sources of information on the velocity and methods for kinematic distance ambiguity resolution (KDAR). We now have velocities of the dense gas traced best by $H^{13}CO^+$ or HCO^+ (see later section), and there are newer distance estimators. We recalculated the distances using the tool described in Wenger et al. (2018), which provides a distance probability density function (pdf) and two-sided uncertainties. While we use the two-sided uncertainties, they are in general

Table 1
Sample of Clouds

Source	d (kpc)	KDAR	Size (pc)	Log $M_{\rm cloud}$ ($M_\odot$)	Log $M_{\rm dense}$ ($M_\odot$)	Log SFR ($M_\odot$ Myr^{-1})	Map Size ($' \times '$)	^{13}CO Lim (K)	Note
G034.158+00.147	$3.48^{+0.43}_{-0.32}$	N	$22.68^{+2.80}_{-2.09}$	$4.75^{+0.17}_{-0.25}$	$4.13^{+0.10}_{-0.09}$	$2.44^{+0.10}_{-0.10}$	30 × 30	2.2	
G034.997+00.330	$10.43^{+0.38}_{-0.41}$	F	$35.41^{+1.29}_{-1.39}$	$5.52^{+0.15}_{-0.23}$	$4.08^{+0.15}_{-0.23}$	$1.85^{+0.05}_{-0.06}$	10 × 20	2.6	1
G036.459−00.183	$8.68^{+0.56}_{-0.60}$	F	$17.21^{+1.11}_{-1.19}$	$4.96^{+0.15}_{-0.24}$	$3.49^{+0.15}_{-0.23}$	$1.36^{+0.07}_{-0.08}$	14 × 22	2.2	1
G037.677+00.155	$6.60^{+0.13}_{-0.14}$	T	$27.15^{+0.53}_{-0.58}$	$5.45^{+0.15}_{-0.23}$	$3.02^{+0.16}_{-0.25}$	$2.09^{+0.04}_{-0.05}$	10 × 26	1.9	
G045.825−00.291	$8.31^{+0.46}_{-0.62}$	F	$25.69^{+1.42}_{-1.92}$	$5.41^{+0.15}_{-0.24}$	$3.91^{+0.15}_{-0.24}$	$1.87^{+0.06}_{-0.09}$	30 × 30	1.6	
G046.495−00.241	$3.71^{+0.68}_{-0.60}$	N	$8.27^{+1.52}_{-1.34}$	$4.38^{+0.19}_{-0.32}$	$2.85^{+0.19}_{-0.32}$	$1.81^{+0.14}_{-0.18}$	20 × 10	1.6	

Note. (1) Mapped in equatorial coordinates.

fairly symmetric. We use the same choice of near, far, or tangent point distances as Anderson et al. (2014; noted by N, F, or T in the KDAR column of Table 1). In particular, G037.677 +00.155 was placed at the tangent point because its velocity was within 10 km s^{-1} of the velocity at the tangent point. We have scaled the sizes, cloud masses, dense gas masses, and star formation rates to the new distances and propagated the uncertainties in the distance to uncertainties in other quantities. The distance uncertainties typically dominate if they enter the calculation of a quantity. We use the star formation rates from the mid-infrared emission. The results are in Table 1. As discussed in detail in the Appendix, we use the kinematic distance to G034.158+00.147 rather than the closer distance from maser parallax. The latter is quite uncertain and would require an unreasonably large (40 km s^{-1}) peculiar motion.

3. Observations

We mapped the six clouds in the HCN (1−0) (88.631847 GHz; DeLucia & Gordy 1969) and HCO$^+$ (1−0) (89.188526 GHz; Sastry et al. 1981) lines simultaneously using the SEQUOIA array with 16 pixels in a 4 × 4 array at the 14 m telescope of the Taeduk Radio Astronomy Observatory (TRAO; Roh & Jung 1999; Jeong et al. 2019). The observations were conducted by the on-the-fly (OTF) technique in the absolute position switching mode with OFF positions checked to be free from appreciable emission. The mapped areas were different for the individual clouds (Table 1). G034.997+00.330 and G036.459−00.183 were mapped in equatorial coordinates occasionally between 2017 February and May, while the others were mapped in Galactic coordinates between 2018 January and April. The backend was a 2G FFT spectrometer that can accept 32 signal streams at the same time. Thus, it is possible to observe two transitions simultaneously between 85 and 100 GHz or 100 and 115 GHz. The backend bandwidth is 62.5 MHz with 4096 channels, yielding a velocity resolution of 0.05 km s^{-1}. The observed line temperature was calibrated on the $T_{\rm A}^*$ scale by the standard chopper wheel method. We checked the telescope pointing and focus every 3 hr by observing strong SiO maser sources at 86 GHz. The pointing accuracy was better than 10″. The system temperatures depended on the weather conditions and source elevation. They were usually around 200 K during the observing runs. The rms noise levels of the observed spectra were typically about 0.1 K after smoothing to 0.2 km s^{-1} resolution. We smoothed the data with the boxcar function to a velocity resolution of about 0.2 km s^{-1} when fitting line profiles, but some analysis of the data cubes was done with the original resolution. To assess optical depth effects, we observed the innermost footprint in the lines of H^{13}CN and H^{13}CO$^+$ with the same method and rms noise.

The TRAO telescope is the same model as the FCRAO telescope. The panels were readjusted and the radome was replaced before our observations were taken. The resulting instrumental properties are described in Jeong et al. (2019). The TRAO has a main-beam size of 58″ and a main-beam efficiency of 46% at 89 GHz. The individual SEQUOIA beams vary in beam size (efficiency) by only a few arcseconds (few percent). The beams are very circular; variation of efficiency with elevation is less than 3%.

Many of our sources are quite extended, so the efficiency on the Moon is more relevant for some. This has not yet been measured for the TRAO, but it should be at least as high as that of the FCRAO, where $\eta_{\rm Moon} = 0.7$. The error beam has not been measured for the TRAO, but it should be no worse than that of the FCRAO. There are two error beams for the FCRAO: one is caused by the radome and the other by small-scale irregularities on the panels. The radome error beam is spread over 4° at −30 dB (0.1%), too weak and diffuse to be an issue here. The panel error beam has a size of 30′ at −18 dB (1.6%). We will assess whether this error beam could affect our results in Section 5.2.1.

4. Results

The most compact presentation of the results is in Figures 1–6. In each figure, all panels present the outermost contour of the velocity integrated intensity of ^{13}CO emission with four tracers of dense gas (in color) superimposed: (1) the $A_{\rm V} > 8$ mag mask based on the ^{13}CO column density, (2) the millimeter-wave continuum emission from BGPS, (3) the HCN integrated intensity, and (4) the HCO$^+$ integrated intensity. (The method used to determine the $A_{\rm V} > 8$ mask is described in Section 5.1.) Two panels show in color the column density determined from Herschel data and the radio continuum emission.

Inspection reveals a considerable range of behavior. G034.158+00.147 and G034.997+00.330 show strong emission from both line tracers and BGPS, and all tracers agree qualitatively on the location of the dense gas. At the other extreme, G037.677+00.155 has only very weak emission from either dense line tracer, both concentrated in the upper right corner of the ^{13}CO map; G037.677+00.155 has weak ^{13}CO emission and no regions with $A_{\rm V} > 8$ mag. G036.459−00.183 and G045.825−00.291 have weak emission from the dense line tracers that is more extended and poorly correlated with the BGPS and $A_{\rm V} > 8$ mag indicators. G046.495−00.241 has three, often overlapping, velocity components that complicate

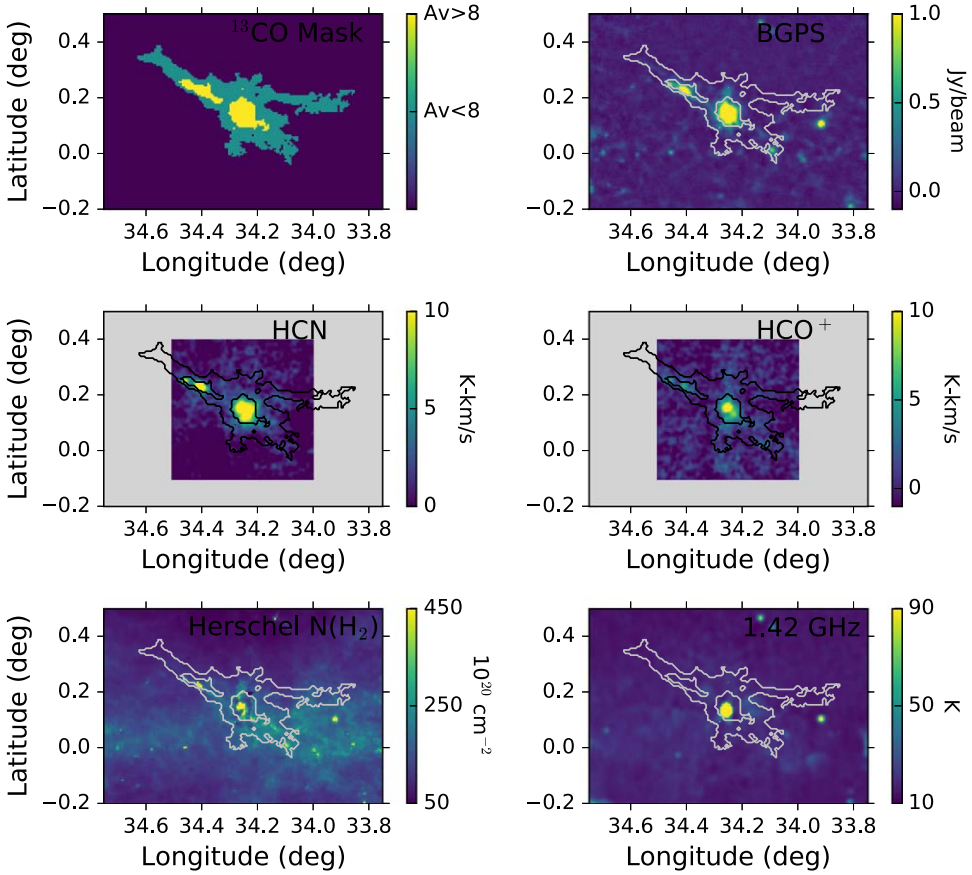

Figure 1. This figure is for the cloud G034.158+00.147. Except for the upper left panel, the GRS ^{13}CO contours are shown in black or white, depending on the panel, along with images of other tracers or masks. The upper left panel shows the mask for column density $A_V \geqslant 8$ mag and the outermost contour of ^{13}CO emission. The upper right panel shows the BGPS millimeter-wave continuum emission in color with the ^{13}CO contour in white. The center left panel shows the HCN integrated intensity in color with the ^{13}CO contour in black. The center right panel shows the HCO$^+$ integrated intensity in color with the ^{13}CO contour in black. The lower left panel shows the gas column density determined from Herschel in color with the ^{13}CO contour in white. The lower right panel shows the 1.42 GHz radio continuum emission in color with the ^{13}CO contour in white. The size of the box in the center panels shows the region mapped in HCN and HCO$^+$. ^{13}CO is in units of K km s^{-1} (T_{mb}) scaled 0–50 K km s^{-1}. The color bars indicate the range and scaling of the other tracers.

analysis, but in general, it shows moderate agreement among the various tracers of dense gas. More complete results for each cloud (spectra at peaks, contour diagrams of integrated intensity, etc.) are provided in the Appendix.

5. Analysis

5.1. Tracer Comparison

We quantify the results from the visual comparison in Section 4, focusing on the fraction of the luminosity of the line tracers that comes from regions indicated to be dense, based on extinction or millimeter-wave continuum emission. This section is geared toward understanding how the line tracers will behave when clouds are observed with spatial resolutions much greater than 1 pc, as in observations of other galaxies. Thus, we do not separate emission from clumps that differ in spatial or velocity location. That analysis is presented in Section 5.2.

First, we describe the method used to make the maps of column density and the $A_V > 8$ mag mask. CO (our convention is that the most common isotope is indicated unless otherwise specified) and ^{13}CO data were used to define column density maps for each target. The procedure to convert these data into ^{13}CO column densities for this paper was largely described by Ripple et al. (2013). In short, we used Equations (1)–(5) of Ripple et al. (2013) to calculate the column density of ^{13}CO, assuming low to moderate optical depths of ^{13}CO emission and optically thick CO emission. Monte Carlo simulations are computed to derive the excitation temperature and ^{13}CO column density and corresponding uncertainties generated by the thermal noise of the data. We then converted to molecular hydrogen by assuming an isotopic ^{12}C/^{13}C ratio of 45 (Milam et al. 2005) and fractional abundance of 6000 for CO, based on a recent determination of the CO abundance by Lacy et al. (2017). Our conversion to extinction of $A_V = 1.0 \times 10^{-21} N(H_2)$ is also provided by Lacy et al. (2017). Fractionation could decrease the ratio of CO to ^{13}CO, which would cause us to overestimate the column density with our assumed isotopic ratio, but we have no good method to correct for this, and the effect is not large in these relatively warm clouds.

The much higher threshold of 1 g cm^{-2} proposed by McKee & Tan (2003) to avoid fragmentation and favor the formation of massive stars is not probed by ^{13}CO emission, so we used the column density determined from Herschel data (Marsh et al. 2017) and available at the HIGAL site: http://www.astro.cardiff.ac.uk/research/ViaLactea/. We do not use the Herschel data for regions of more modest column density because foreground/background emission strongly contaminates it. It traces only the highest column density regions accurately in the inner Galaxy.

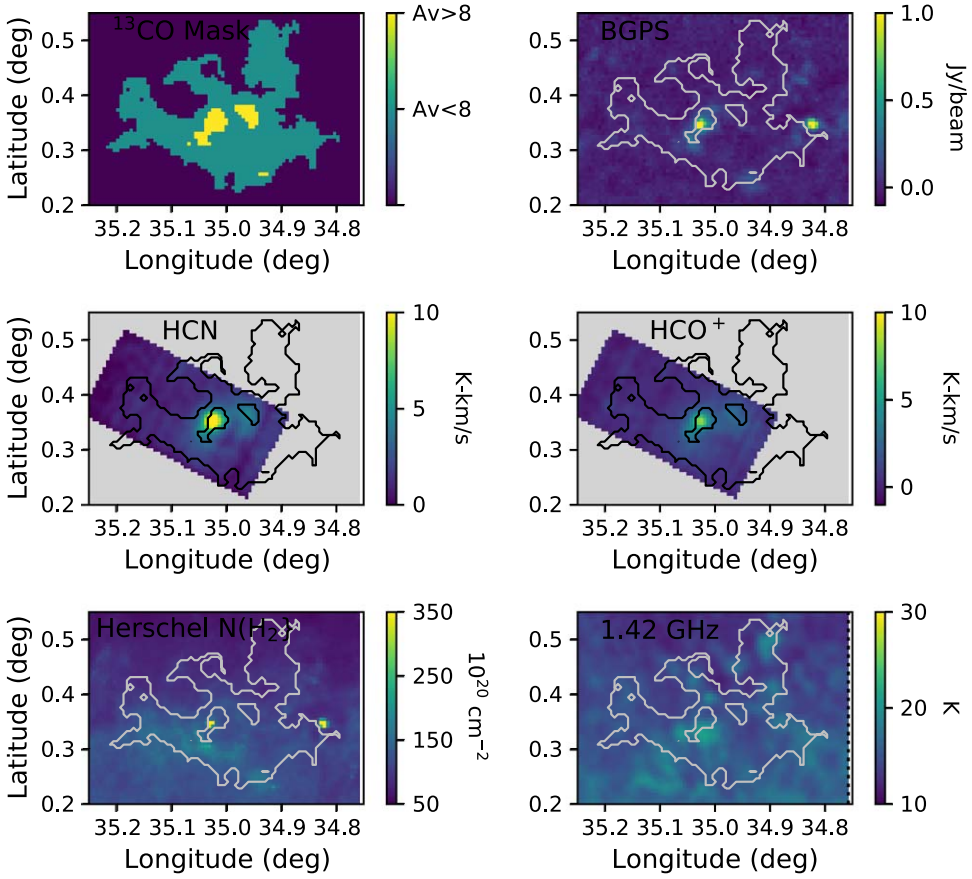

Figure 2. This figure is for the cloud G034.997+00.330. Except for the upper left panel, the GRS ^{13}CO contours are shown in black or white, depending on the panel, along with images of other tracers or masks. The upper left panel shows the mask for column density $A_V \geqslant 8$ mag and the outermost contour of ^{13}CO emission. The upper right panel shows the BGPS millimeter-wave continuum emission in color with the ^{13}CO contour in white. The center left panel shows the HCN integrated intensity in color with the ^{13}CO contour in black. The center right panel shows the HCO$^+$ integrated intensity in color with the ^{13}CO contour in black. The lower left panel shows the gas column density determined from Herschel in color with the ^{13}CO contour in white. The lower right panel shows the 1.42 GHz radio continuum emission in color with the ^{13}CO contour in white. The size of the box in the center panels shows the region mapped in HCN and HCO$^+$. ^{13}CO is in units of K km s^{-1} (T_{mb}) scaled 0–50 K km s^{-1}. The color bars indicate the range and scaling of the other tracers.

These maps of column density were used to define the regions of column density corresponding to various thresholds used to define "dense" gas. The velocity interval of ^{13}CO emission was used to limit the range of velocities of plausible emission from HCO$^+$; the range was extended for HCN to account for hyperfine splitting. Then, the data cubes for ^{13}CO, BGPS, and Herschel column densities were convolved, resampled, and aligned with the TRAO maps. These were used to measure the luminosity inside and outside the region defined by the criterion described above. This allowed us to determine what fraction of the HCN and HCO$^+$ emission arose from "dense" gas, as defined by that criterion. In this section, the main-beam efficiency has been used to correct to the scale of T_{mb}. This procedure may overestimate the brightness for very extended emission.

The luminosity inside and outside regions defining various indicators of dense gas are discussed in the following sections. The integration of luminosity is limited to the intersection of the ^{13}CO-defined cloud and the mapping box from the TRAO observations for both HCN and HCO$^+$ but not for ^{13}CO. The equations used to compute the luminosity follow:

$$L_{X,\mathrm{in}} = D^2 \int dv \int d\Omega_{\mathrm{in}} T_X(l, b, v), \quad (1)$$

and

$$L_{X,\mathrm{out}} = D^2 \int dv \int d\Omega_{\mathrm{out}} T_X(l, b, v), \quad (2)$$

where X refers to the tracer, D is the distance in parsecs, and Ω_{in} and Ω_{out} are the solid angle of pixels that satisfy (in) or do not satisfy (out), respectively, one of the given conditions (column density from ^{13}CO, column density from Herschel emission, or overlap with the mask of emission from the BGPS). In practice, a summed spectrum was constructed from all pixels that satisfied the conditions. The uncertainties were calculated as follows: the rms noise of the summed spectrum ($\mathrm{rms}_{\mathrm{sum}}$) is the quadrature sum of rms noise values of each pixel that satisfies the threshold condition. The uncertainty in the luminosity is then

$$\mathrm{rms}_{\mathrm{L}} = \delta v \sqrt{N_{\mathrm{ch}}}\, \mathrm{rms}_{\mathrm{sum}} d\Omega D^2 \quad (3)$$

where δv is the channel width, and N_{ch} is the number of channels in the integration range. In most sources, these uncertainties were quite small compared to the luminosity, reflecting the fact that they included only the uncertainties in the summed spectrum. The distance uncertainties (Table 1)

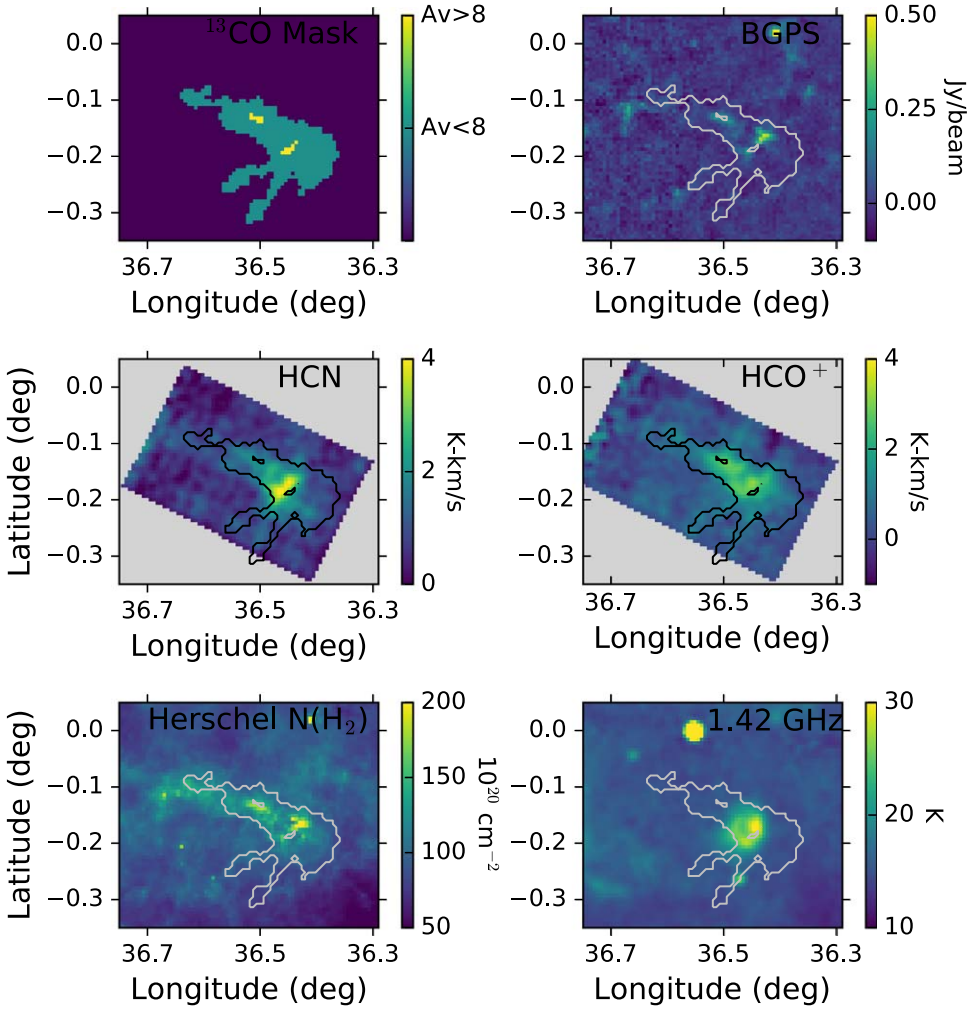

Figure 3. This figure is for the cloud G036.459−00.183. Except for the upper left panel, the GRS ^{13}CO contours are shown in black or white, depending on the panel, along with images of other tracers or masks. The upper left panel shows the mask for column density $A_V \geqslant 8$ mag and the outermost contour of ^{13}CO emission. The upper right panel shows the BGPS millimeter-wave continuum emission in color with the ^{13}CO contour in white. The center left panel shows the HCN integrated intensity in color with the ^{13}CO contour in black. The center right panel shows the HCO$^+$ integrated intensity in color with the ^{13}CO contour in black. The lower left panel shows the gas column density determined from Herschel in color with the ^{13}CO contour in white. The lower right panel shows the 1.42 GHz radio continuum emission in color with the ^{13}CO contour in white. The size of the box in the center panels shows the region mapped in HCN and HCO$^+$. ^{13}CO is in units of K km s^{-1} (T_{mb}) scaled 0–50 K km s^{-1}. The color bars indicate the range and scaling of the other tracers.

were added in quadrature for all luminosities but not for ratios of luminosities, for which the distance cancels out.

5.1.1. Line Tracers versus the Extinction Criterion

How much of the luminosity of the line tracers arises within regions satisfying the extinction criterion ($A_V > 8$ mag)? While our main focus is on HCN and HCO$^+$, we consider ^{13}CO as well because its emission is stronger and easier to obtain for other galaxies.

We used the procedure described above to determine the luminosity of each tracer for regions with column density above and below that threshold, as measured by the ^{13}CO column density. The values for the fraction of pixels inside the A_V criterion, the log of the total line luminosity, and the fraction of the total arising inside the $A_V > 8$ mag region ($f_L = L_{in}/L_{tot}$) are listed for HCN, HCO$^+$, and ^{13}CO in Table 2. Two-sided errors are given for the logarithmic luminosities, which are dominated by the distance uncertainties. The distance does not enter in the f_L values, so the uncertainties are symmetric, much smaller, and given in parentheses. The mean, standard deviation, and median are given for the relevant columns. Since G037.677+00.155 had no pixels above the criterion, its value for f_L is zero for all three tracers. The values of f_L vary widely, with f_L between 0 and 0.54 for HCN, between 0 and 0.56 for HCO$^+$, and between 0 and 0.33 for ^{13}CO. HCN and HCO$^+$ give very similar results for f_L. In terms of the total line luminosities, the mean of the logarithms of L_{tot} is higher by 0.25 for HCN compared to HCO$^+$. So, the two dense line tracers provide similar measures in this sample, but the luminosity of HCN is somewhat higher than that of HCO$^+$. ^{13}CO provides still higher luminosity but a worse correlation with the extinction criterion for the first two clouds and a similar correlation for the others.

Does the fraction of line luminosity arising at high column density correlate with any observable properties? Figure 7 plots f_L versus total line luminosity; no trend is apparent. Neither is there a strong trend of increasing f_L with SFR (Figure 8). While the highest values of f_L correspond to the cloud with the highest star formation rate, the other clouds do not support an overall trend.

Finally, we comment on the absence of any gas with $A_V > 8$ mag in G037.677+00.155. It is a large (27 pc) and

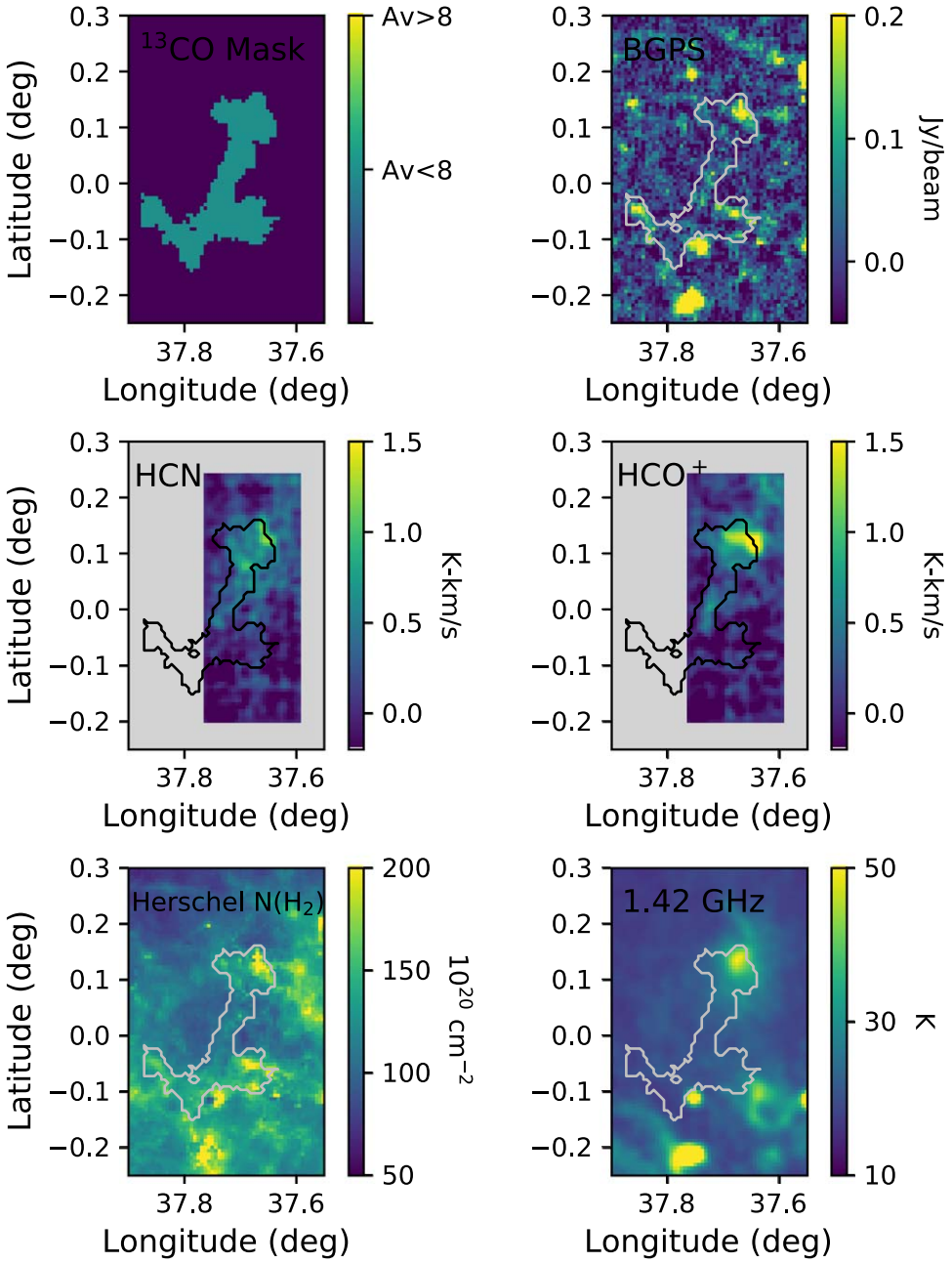

Figure 4. This figure is for the cloud G037.677+00.155. Except for the upper left panel, the GRS ^{13}CO contours are shown in black or white, depending on the panel, along with images of other tracers or masks. The upper left panel shows the mask for column density $A_V \geqslant 8$ mag and the outermost contour of ^{13}CO emission. The upper right panel shows the BGPS millimeter-wave continuum emission in color with the ^{13}CO contour in white. The center left panel shows the HCN integrated intensity in color with the ^{13}CO contour in black. The center right panel shows the HCO$^+$ integrated intensity in color with the ^{13}CO contour in black. The lower left panel shows the gas column density determined from Herschel in color with the ^{13}CO contour in white. The lower right panel shows the 1.42 GHz radio continuum emission in color with the ^{13}CO contour in white. The size of the box in the center panels shows the region mapped in HCN and HCO$^+$. ^{13}CO is in units of K km s^{-1} (T_{mb}) scaled 0–50 K km s^{-1}. The color bars indicate the range and scaling of the other tracers.

massive (log $M_{cloud} = 5.45$) cloud, with the second highest SFR in the sample. The absence of regions with $A_V > 8$ mag and only weak, fragmented emission in dense gas tracers is thus surprising, except that the fraction of dense gas indicated by the BGPS emission (3.7×10^{-3}) was the lowest in the sample. This cloud is probably more evolved, with the current episode of star formation coming to an end.

5.1.2. Line Tracers versus the 1 g cm^{-2} Criterion

McKee & Tan (2003) proposed the criterion of a surface density of 1 g cm^{-2} for efficient formation of massive stars. ^{13}CO does not trace such high column densities, so we used the column density from the Herschel data, as described in Section 5.1. There is a small region (10 pixels) in G034.158+00.147 and a single pixel in G034.997+00.330 that meet the criterion. The fractions of the HCN luminosity in those regions are 0.034 for G034.158+00.147 and 0.006 in G034.997+00.330. For HCO$^+$, the equivalent fractions are 0.046 and 0.006; for ^{13}CO, they are 0.019 and 0.0. (For ^{13}CO, no pixels were inside that region in G034.997+00.330, presumably because of slightly different sampling.) These numbers are interestingly small; the criterion was originally formulated in

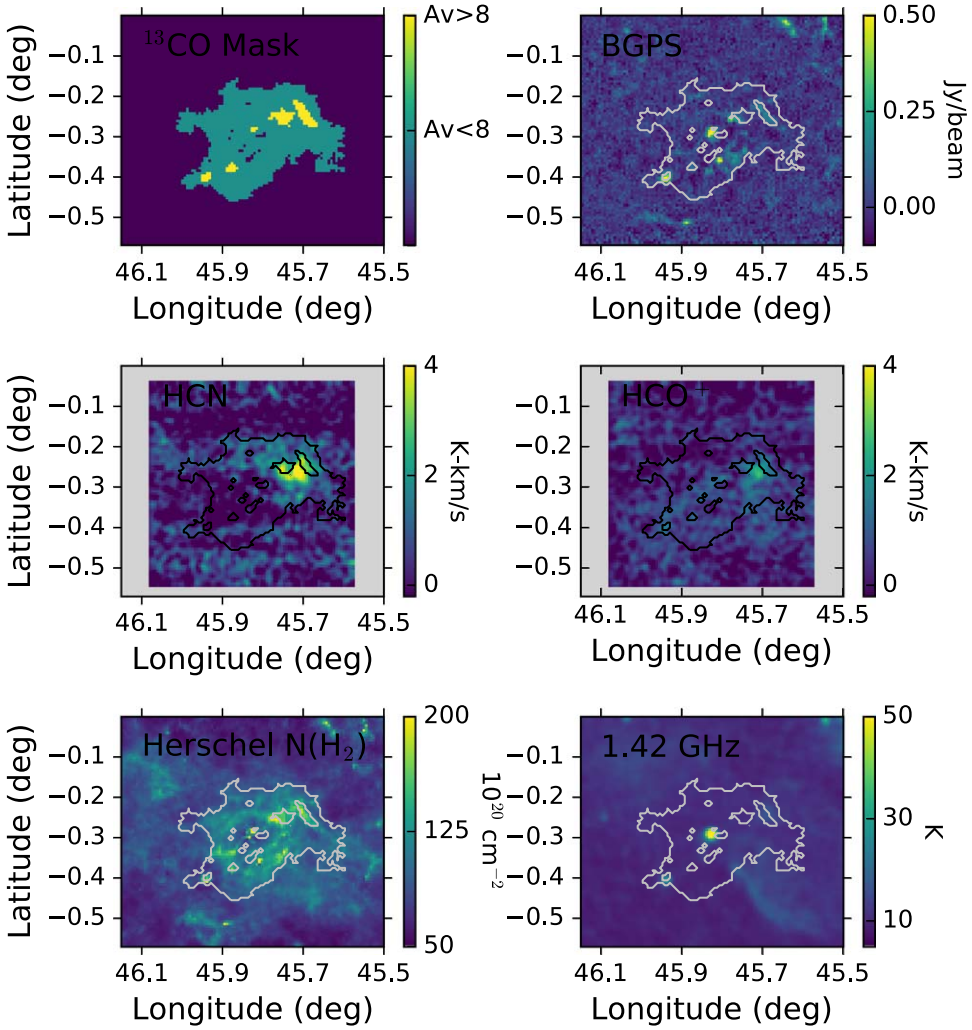

Figure 5. This figure is for the cloud G045.825−00.291. Except for the upper left panel, the GRS ^{13}CO contours are shown in black or white, depending on the panel, along with images of other tracers or masks. The upper left panel shows the mask for column density $A_V \geqslant 8$ mag and the outermost contour of ^{13}CO emission. The upper right panel shows the BGPS millimeter-wave continuum emission in color with the ^{13}CO contour in white. The center left panel shows the HCN integrated intensity in color with the ^{13}CO contour in black. The center right panel shows the HCO$^+$ integrated intensity in color with the ^{13}CO contour in black. The lower left panel shows the gas column density determined from Herschel in color with the ^{13}CO contour in white. The lower right panel shows the 1.42 GHz radio continuum emission in color with the ^{13}CO contour in white. The size of the box in the center panels shows the region mapped in HCN and HCO$^+$. ^{13}CO is in units of K km s^{-1} (T_{mb}) scaled 0–50 K km s^{-1}. The color bars indicate the range and scaling of the other tracers.

the context of the early work on dense clumps identified with strong localized emission by CS $J = 7 \rightarrow 6$, (Plume et al. 1997) similar in spirit to the HCN and HCO$^+$ line tracers but much more biased toward very high densities. The sample of Plume et al. (1997) was originally based on sources with water masers. As far as we know, G034.158+00.147 is the only source in our sample with a water maser. A recent study of the M17 cloud found that neither HCN nor HCO$^+$ $J = 1 \rightarrow 0$ was particularly good at distinguishing regions above this criterion (Nguyen-Luong et al. 2020). Higher J transitions are needed to probe such regions (Wu et al. 2010).

5.1.3. Line Tracers versus BGPS Emission

Vutisalchavakul et al. (2016) used the millimeter-wave continuum emission from the BGPS survey to estimate the mass of dense gas. To test how well the line tracers correlate with that criterion for "dense", we also computed the line luminosities inside and outside the mask supplied by the BGPS catalog. In the mask file, each pixel is set to zero if no emission was detected or to the catalog number of the source if emission was significant (Ginsburg et al. 2013).

As can be seen from Figure 5, G045.825−00.291 has very little overlap between the BGPS emission and the HCN/HCO$^+$ emission. Consequently, the values in the table for that source are effectively upper limits. For the remaining four sources, the correlation with BGPS is reasonably strong, as captured in f_L for BGPS in Table 3. As for the extinction criterion, the two dense line tracers agree well, but the luminosity of HCN is greater by 0.25 in the log on average. The f_L values for ^{13}CO are more comparable to the dense line tracers than was the case for the extinction criterion. This reflects the fact that the BGPS emission from distant clouds traces a lower average density than it traces in nearby clouds, so that it begins to trace structures between the scale of clouds and dense clumps beyond distances of 5–10 kpc (Dunham et al. 2011). Thus, ^{13}CO, HCN, and HCO$^+$ all seem to trace the gas inferred from the BGPS data similarly. Since Vutisalchavakul et al. (2016) used BGPS to measure dense gas mass, we would expect their values of SFR per unit mass to be lower than those for the

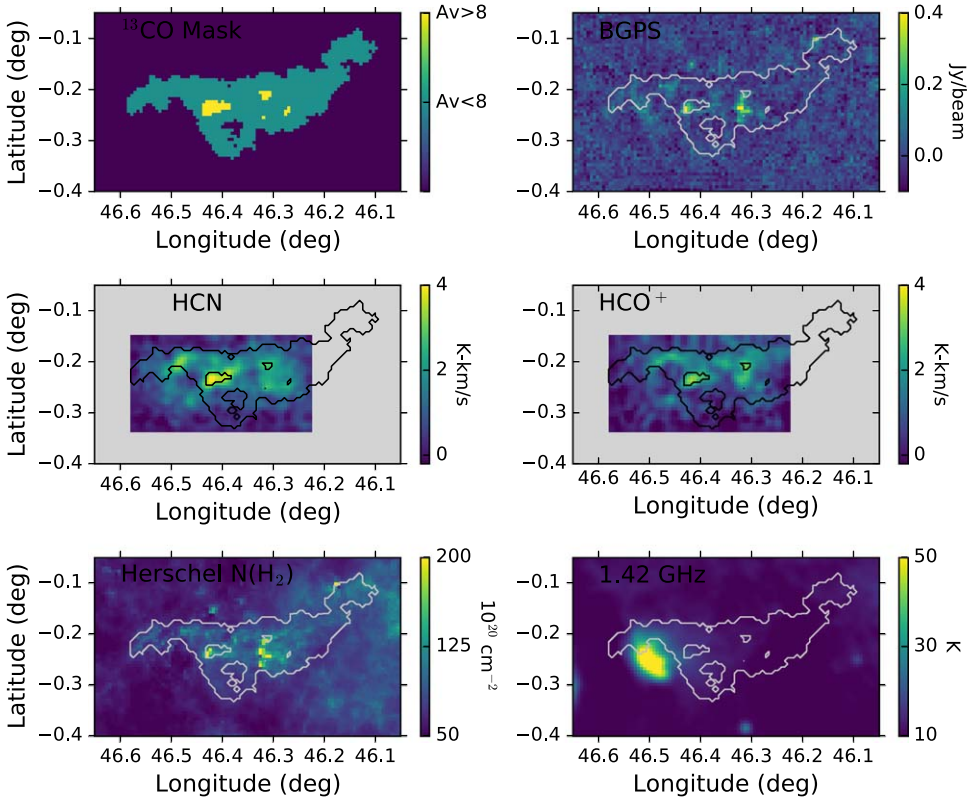

Figure 6. This figure is for the cloud G046.495−00.241. Except for the upper left panel, the GRS ^{13}CO contours are shown in black or white, depending on the panel, along with images of other tracers or masks. The upper left panel shows the mask for column density $A_V \geqslant 8$ mag and the outermost contour of ^{13}CO emission. The upper right panel shows the BGPS millimeter-wave continuum emission in color with the ^{13}CO contour in white. The center left panel shows the HCN integrated intensity in color with the ^{13}CO contour in black. The center right panel shows the HCO$^+$ integrated intensity in color with the ^{13}CO contour in black. The lower left panel shows the gas column density determined from Herschel in color with the ^{13}CO contour in white. The lower right panel shows the 1.42 GHz radio continuum emission in color with the ^{13}CO contour in white. The size of the box in the center panels shows the region mapped in HCN and HCO$^+$. ^{13}CO is in units of K km s^{-1} (T_{mb}) scaled 0–50 K km s^{-1}. The color bars indicate the range and scaling of the other tracers.

nearby clouds, where the $A_V > 8$ mag criterion can be used. Indeed, this was the case.

5.1.4. Conversion of Line Tracer Luminosity to Mass of Dense Gas

We also plot the mass of dense gas determined from BGPS versus the luminosity of HCN in Figure 9 for both the total line tracer luminosity and the line tracer luminosity inside the BGPS mask. Both correlate, but the correlation is better for L_{in}. The values of M_{dense}, L_{in}, and both conversion factors $\alpha_{in} = M_{dense}/L_{in}$ and $\alpha_{tot} = M_{dense}/L_{tot}$ are tabulated in Table 4 for both HCN and HCO$^+$, along with the means, standard deviations, and medians.

While the BGPS emission is tracing a somewhat lower-density material than the $A_V > 8$ mag criterion for the distant clouds, it has still been used to trace dense gas, so a conversion factor between the dense line tracers and the mass determined from BGPS is of interest. If we restrict the luminosity of HCN to the region inside the BGPS mask, we get $\langle \log(\alpha_{in}) \rangle = 1.308 \pm .254$, translating to $M_{dense} = 20^{+16}_{-9}$ L(HCN). Including the luminosity of the entire cloud, the result is $\langle \log(\alpha_{tot}) \rangle = 0.793 \pm .315$, translating to $M_{dense} = 6.2^{+6.6}_{-3.0}$ L(HCN). The latter value is more appropriate for extragalactic observations, where the luminosity will arise from the whole cloud if one wants to estimate the mass of material with densities similar to that of BGPS sources in the Galaxy. A conversion factor of 20 (appropriate for the luminosity inside the BGPS mask) is the same as the average of 20 ± 5 derived by Wu et al. (2010) while the value of 6.2 is more similar to, but a bit lower than, that used in extragalactic studies (Gao & Solomon 2004; Liu et al. 2015; Jiménez-Donaire et al. 2019).

5.1.5. HCO$^+$ versus HCN versus ^{13}CO

The fraction of luminosity coming from the $A_V > 8$ mag region is plotted for each of the line tracers in Figure 10. The first two clouds (G034.158+00.147 and G034.997+00.330) clearly differ from the other four. The values for f_L are higher, and those for HCN or HCO$^+$ clearly exceed those for ^{13}CO. For the other four, all of the values are low, and the different tracers are in rough agreement. In those clouds, the ^{13}CO would be equally good or bad at tracing the dense gas.

The ratio of total luminosities, L(HCO$^+$)/L(HCN), averaged in the logs, is 0.56, similar to the 0.7 ratio found in the EMPIRE study (Jiménez-Donaire et al. 2019) and in the CMZ of the Galaxy (Jones et al. 2012) as well as the ratio of 0.73 found in M17 (Nguyen-Luong et al. 2020). However, there are substantial variations from cloud to cloud. Despite the differences in critical density, and probably in chemistry as well, the two lines seem to be tracing a similar material on average in this sample. Both lines trace about the same concentration of emission, as measured by f_L. For the $A_V > 8$ mag criterion, the average ratio $\langle f_L(\text{HCO}^+)/f_L(\text{HCN}) \rangle = 1.14 \pm 0.18$. This is not what

Table 2
Line Luminosities vs. $A_V > 8$

Source	N/N_{tot}	Log L_{tot} HCN	f_L HCN	Log L_{tot} HCO^+	f_L HCO^+	Log L_{tot} ^{13}CO	f_L ^{13}CO
G034.158+00.147	0.163	$2.68^{+0.10}_{-0.09}$	0.539 (0.003)	$2.54^{+0.10}_{-0.09}$	0.559 (0.003)	$3.75^{+0.10}_{-0.09}$	0.332 (0.000)
G034.997+00.330	0.079	$3.37^{+0.03}_{-0.04}$	0.251 (0.002)	$3.09^{+0.03}_{-0.04}$	0.243 (0.002)	$4.34^{+0.03}_{-0.04}$	0.125 (0.000)
G036.459−00.183	0.004	$2.95^{+0.06}_{-0.07}$	0.007 (0.000)	$2.81^{+0.05}_{-0.07}$	0.010 (0.000)	$3.86^{+0.05}_{-0.06}$	0.019 (0.000)
G037.677+00.155	0.000	$2.22^{+0.02}_{-0.02}$	0.000 (0.000)	$2.02^{+0.02}_{-0.02}$	0.000 (0.000)	$3.59^{+0.02}_{-0.02}$	0.000 (0.000)
G045.825−00.291	0.054	$3.13^{+0.05}_{-0.07}$	0.148 (0.003)	$2.56^{+0.05}_{-0.07}$	0.169 (0.008)	$3.88^{+0.05}_{-0.07}$	0.113 (0.001)
G046.495−00.241	0.035	$2.36^{+0.14}_{-0.17}$	0.088 (0.002)	$2.20^{+0.14}_{-0.17}$	0.098 (0.002)	$3.34^{+0.14}_{-0.17}$	0.075 (0.000)
Mean	0.056	2.79	0.172	2.54	0.180	3.79	0.111
Std Dev.	0.055	0.41	0.185	0.36	0.190	0.31	0.109
Median	0.045	2.82	0.118	2.55	0.133	3.80	0.094

Note. (1) Units of luminosities are K km s^{-1} pc^2.

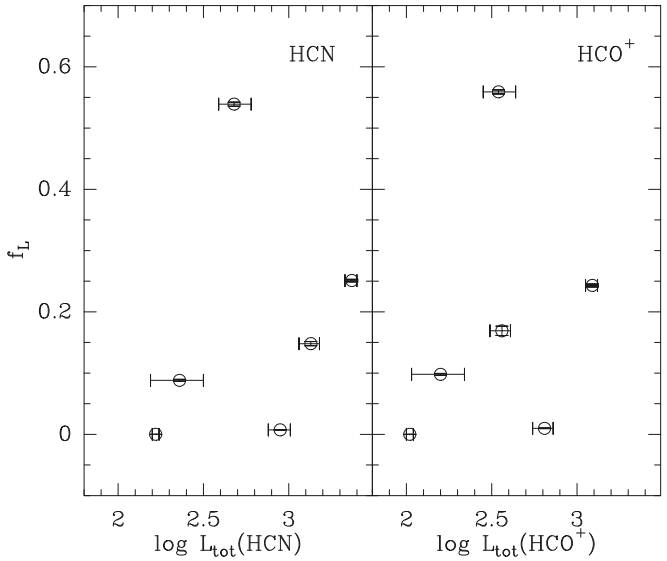

Figure 7. The fraction of line luminosity arising above $A_V > 8$ mag is plotted vs. total line luminosity. HCN is plotted in the left panel and HCO^+ in the right panel.

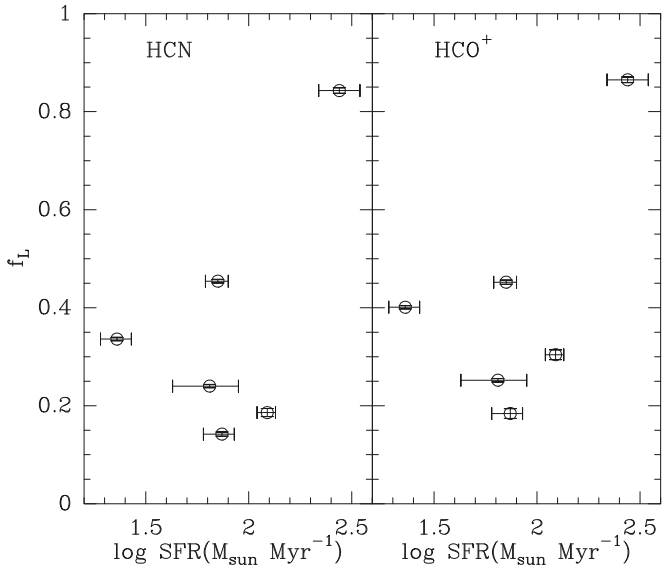

Figure 8. The fraction of line luminosity arising in the BGPS emission region is plotted vs. the star formation rate. HCN is plotted in the left panel and HCO^+ in the right panel.

simplistic predictions based on critical densities would have predicted (see Sections 5.2.1 and 6).

5.2. Clump Analysis

In this section, we search for peaks, separating different velocity components where necessary. This analysis is used to characterize the spectra and sizes of the peaks identified in the line tracers. This analysis shows what can be done with a spatial resolution much less than 1 pc, as is common within the Galaxy.

Our standard procedure is as follows. We examine the data to find all velocity intervals with significant emission. Then, we exclude those regions while removing a second-order baseline, also using only enough of a velocity range to get a good baseline on each end (v_{sp}) and excluding velocities with emission (v_{win}). The values of the total velocity range and excluded windows are shown in Table B1. Then, I, T_A^* integrated over a velocity range (v_I) is computed for every mapped position, regardless of whether a line is detected there. These are plotted in contour diagrams, which are used to define the peak position, find regions that should be eliminated, and find the FWHM size. Contour diagrams are made in steps of 2σ, starting at 2σ, where σ is the rms noise in the integrated intensity (I), as listed in Table B1. Spectra at the peak position, or for cases of weak emission, spectra averaged over nearby positions, were used to determine line properties such as integrated intensity, velocity, and linewidth (Table 5). This was often an iterative process in which the line properties were used to refine the velocity range (v_I) for integrated intensities, and the area outside the 2σ emission regions was refined to determine better noise levels. The values in Table B1 represent the final values.

5.2.1. What Is the Origin of the Line Tracer Luminosity from Low-density Regions?

With a clear identification of the center of emission, we can explore the origin of the luminosity of dense line tracers outside the region of the dust tracers. G034.997+00.330 provides a good test case because there is a single, clearly defined peak in the dense line tracers. In Figure 11, the integrated intensities are sorted by distance from the peak position, normalized to the peak, and plotted versus distance; smoothed versions are also plotted. While both positive and negative values are found at large separations from the peak, there is a positive bias. In this

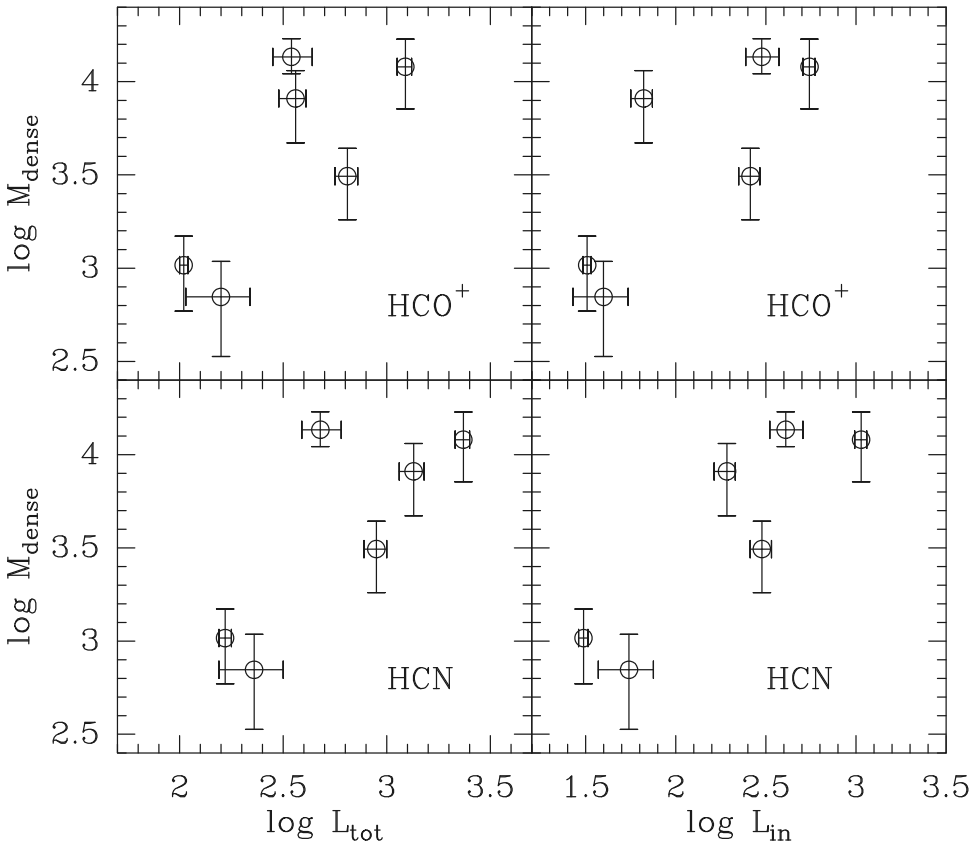

Figure 9. The mass of dense gas determined from BGPS data is plotted vs. the line luminosity. HCN is plotted in the bottom panels and HCO^+ is plotted in the top panels. The total line luminosities are shown in the left panels, and the luminosity inside the BGPS mask is shown in the right panels.

Table 3
Line Luminosities vs. BGPS Emission

Source	$N/N_{\rm tot}$ HCN	Log $L_{\rm tot}$ HCN	$f_{\rm L}$ HCN	Log $L_{\rm tot}$ HCO^+	$f_{\rm L}$ HCO^+	$N/N_{\rm tot}$ ^{13}CO	Log $L_{\rm tot}$ ^{13}CO	$f_{\rm L}$ ^{13}CO
G034.158+00.147	0.625	$2.68^{+0.10}_{-0.09}$	0.843 (0.006)	$2.54^{+0.10}_{-0.09}$	0.865 (0.006)	0.612	$3.75^{+0.10}_{-0.09}$	0.741 (0.001)
G034.997+00.330	0.267	$3.37^{+0.03}_{-0.04}$	0.454 (0.004)	$3.09^{+0.03}_{-0.04}$	0.452 (0.004)	0.261	$4.34^{+0.03}_{-0.04}$	0.344 (0.000)
G036.459−00.183	0.205	$2.95^{+0.05}_{-0.06}$	0.336 (0.004)	$2.81^{+0.05}_{-0.06}$	0.401 (0.003)	0.235	$3.86^{+0.05}_{-0.06}$	0.347 (0.000)
G037.677+00.155	0.189	$2.22^{+0.03}_{-0.03}$	0.186 (0.008)	$2.02^{+0.02}_{-0.02}$	0.304 (0.010)	0.230	$3.59^{+0.02}_{-0.02}$	0.275 (0.001)
G045.825−00.291	0.110	$3.13^{+0.05}_{-0.07}$	0.142 (0.004)	$2.56^{+0.05}_{-0.08}$	0.184 (0.010)	0.116	$3.88^{+0.05}_{-0.07}$	0.141 (0.001)
G046.495−00.241	0.145	$2.36^{+0.14}_{-0.17}$	0.240 (0.004)	$2.20^{+0.14}_{-0.17}$	0.252 (0.004)	0.128	$3.34^{+0.14}_{-0.17}$	0.197 (0.000)
Mean	0.257	2.79	0.367	2.54	0.410	0.264	3.79	0.341
Std Dev.	0.172	0.41	0.236	0.36	0.222	0.165	0.31	0.194
Median	0.197	2.82	0.288	2.55	0.353	0.233	3.80	0.309

Note. (1) Units of luminosities are K km s^{-1} pc^2.

source, roughly 72% of the dense line tracers' luminosity arising outside the $A_V > 8$ mag mask does not arise in secondary weak emission peaks but in very widespread emission that is mostly below the detection threshold in individual spectra ($T_A^* \sim 0.3$ K for a 3σ detection).

Could the error beam discussed above create the illusion of low-level, widespread emission? Smoothly extended emission at a level of 1.6% or less relative to the peaked emission could be caused by the error beam. We estimate the observed ratio by using the data inside and outside the $A_V = 8$ mag contours from Table 2 and the following argument. The surface brightness, $B \propto L/(N\Omega)$, where N is the number of pixels, and Ω is the pixel solid angle. Then,

$$R = B(\text{out})/B(\text{in}) = L(\text{out})/L(\text{in}) \times N(\text{in})/N(\text{out}) = f_{\rm L}^{-1} \times N(\text{in})/N(\text{out}). \quad (4)$$

Approximating N(out) by N(tot), since $N(\text{out}) \gg N(\text{in})$, we use the values in Table 2 to estimate R. The values range from 0.29 to 0.40, much larger than the 0.016 that the error beam could contribute.

The calculation above assumes that the emission is smoothly distributed inside and outside the $A_V = 8$ mag contours. For some sources, the emission is more sharply peaked, so we also

Table 4
$M_{\rm dense}$ vs. Luminosities

Source	Log $M_{\rm dense}$ $M_\odot$	Log $L_{\rm in}$ HCN	Log $\alpha_{\rm in}$ HCN	Log $\alpha_{\rm tot}$ HCN	Log $L_{\rm in}$ HCO^+	Log $\alpha_{\rm in}$ HCO^+	Log $\alpha_{\rm tot}$ HCO^+
G034.158+00.147	$4.13^{+0.10}_{-0.09}$	$2.61^{+0.10}_{-0.09}$	$1.52^{+0.02}_{-0.02}$	$1.45^{+0.02}_{-0.02}$	$2.48^{+0.10}_{-0.09}$	$1.66^{+0.02}_{-0.02}$	$1.59^{+0.02}_{-0.02}$
G034.997+00.330	$4.08^{+0.15}_{-0.23}$	$3.03^{+0.03}_{-0.04}$	$1.05^{+0.15}_{-0.22}$	$0.71^{+0.15}_{-0.22}$	$2.74^{+0.03}_{-0.04}$	$1.34^{+0.15}_{-0.22}$	$0.99^{+0.15}_{-0.22}$
G036.459−00.183	$3.49^{+0.15}_{-0.23}$	$2.48^{+0.05}_{-0.06}$	$1.01^{+0.14}_{-0.22}$	$0.54^{+0.14}_{-0.22}$	$2.41^{+0.05}_{-0.06}$	$1.08^{+0.14}_{-0.22}$	$0.68^{+0.14}_{-0.22}$
G037.677+00.155	$3.02^{+0.16}_{-0.25}$	$1.49^{+0.02}_{-0.03}$	$1.53^{+0.16}_{-0.25}$	$0.80^{+0.16}_{-0.25}$	$1.51^{+0.02}_{-0.02}$	$1.51^{+0.16}_{-0.25}$	$0.99^{+0.16}_{-0.25}$
G045.825−00.291	$3.91^{+0.15}_{-0.24}$	$2.28^{+0.05}_{-0.07}$	$1.63^{+0.14}_{-0.22}$	$0.78^{+0.14}_{-0.22}$	$1.82^{+0.05}_{-0.07}$	$2.09^{+0.14}_{-0.22}$	$1.35^{+0.15}_{-0.22}$
G046.495−00.241	$2.85^{+0.19}_{-0.32}$	$1.74^{+0.14}_{-0.17}$	$1.11^{+0.15}_{-0.23}$	$0.49^{+0.15}_{-0.23}$	$1.60^{+0.14}_{-0.17}$	$1.25^{+0.15}_{-0.23}$	$0.65^{+0.15}_{-0.23}$
Mean	3.579	2.271	1.308	0.793	2.094	1.486	1.044
Std. Dev.	0.505	0.521	0.254	0.315	0.471	0.326	0.339
Median	3.701	2.381	1.314	0.743	2.118	1.423	0.992

Note. (1) Units of luminosities are K km s^{-1} pc^2.

divide the average emission in the region outside the $A_V = 8$ mag contours by the peak emission (Table 5). These ratios range from 5% to 14%, with the exception of G034.158 +00.147, for which the ratio is 0.7%. For all but G034.158 +00.147, the ratio is greater than could be explained by an error beam. The value for G034.158+00.147 is considerably less than the predicted contribution from the error beam, a fact that could be explained if the TRAO error beam is actually lower than that of the FCRAO or by the fact that the ^{13}CO map did not cover the full error beam. To summarize, the extended emission from G034.158+00.147 could arise from the error beam, but none of the other clouds' extended emission could so arise. Having ruled out error beam contributions, we can use the spectra averaged over the whole region outside the $A_V > 8$ mag region to determine the properties of the extended emission. For all but G034.997+00.330, the characteristic $T_{\rm mb}$ ranges from 0.01 to 0.03 K. If this emission is truly distributed, we can use RADEX (van der Tak et al. 2007) to determine the density of colliders needed to produce such weak lines. The results are shown in Figure 12. The dependence of $T_{\rm mb}$ on density is linearly dependent on the density of colliders in this optically thin, low-density regime because every collisional excitation leads to emission of a photon (Liszt & Pety 2016). Because the observations of HCO^+ and HCN show nearly equal line strengths, we adjusted the abundance to produce that result. For HCO^+, we used $N(HCO^+) = 1 \times 10^{13}$ cm^{-2}, and for HCN, $N(HCN) = 2 \times 10^{14}$ cm^{-2}. For total column density, $N = 1 \times 10^{21}$ cm^{-2}, corresponding to about $A_V = 1$ mag, these would correspond to $X = 1 \times 10^{-8}$ for HCO^+, and $X = 2 \times 10^{-7}$ for HCN. Higher total column densities would allow for lower abundances. Such abundances are not unreasonable for extinctions of a few, as indicated by Figure 8 of Goldsmith & Kauffmann (2017). For both, we assumed $T_K = 20$ K and a linewidth of 1 km s^{-1}. These results illustrate that the low-level, very extended emission that can dominate the total luminosity can arise in gas with densities as low as 50–100 cm^{-3}. These densities are similar to the average densities ($\bar{n}$) of the entire cloud, determined by dividing the mass by the volume; for the clouds in this sample, the mean value of this average density, $\langle \bar{n} \rangle = 96 \pm 64$ cm^{-3} (Vutisalchavakul et al. 2016). This is a clear demonstration that common statements about dense gas tracers are too naive, as discussed further in Section 6.

5.2.2. Properties of the Dense Clumps Identified by the Line Tracers

In this section, we derive the properties of the dense clumps, as separated in position and velocity in order to compare them to the properties of the dense clumps studied by Wu et al. (2010). This analysis addresses the question of whether we are comparing apples to oranges. For this purpose, we follow the procedure in Wu et al. (2010). This procedure requires the integrated line intensity (I) and linewidth (Δv) at the peak position, the FWHM angular size of the emission, and the distance.

We use the spectrum of the line at the peak, or in the case of weak lines that are fairly uniformly distributed, an average over spectra surrounding the peak, to obtain the intensity and linewidth. We use the linewidth from HCO^+ or $H^{13}CO^+$ also for the HCN analysis to avoid issues caused by hyperfine structure of HCN. When the lines of the $H^{13}CO^+$ were strong enough, we used them to get the linewidth, following Wu et al. (2010). This was possible only for G034.158+00.147 and G034.997+00.330.

We find the angular size of the source at the FWHM of the integrated intensity map. The FWHM source size is determined by plotting the 50% contour and determining the geometric mean of the two dimensions. This involves some judgment for weakly peaked regions, and some "peninsulas" were ignored. The uncertainties in the angular size were assessed by repeating the procedure for the 40% and 60% contours; as a result, we included an uncertainty of 20″ for the angular size in the next steps. The source sizes were generally much larger than the beam size, indicating that beam dilution was a minor effect. The most compact source, G034.158+00.147, had a source size of 87″, much larger than the beam size. While there is undoubtedly structure smaller than our beam, it would have a small effect on the following analysis, which is intended to compare our results to those of Wu et al. (2010), who used the FCRAO for $J = 1 \rightarrow 0$ observations, hence, the same beam size on comparably distant sources. The method for deriving source sizes was chosen to be similar to that used by Wu et al. (2010). While crude and somewhat subjective, it provided the most sensible results.

This angular size of the source, corrected for beam size, determines the properties of the dense gas, as defined by the line tracers themselves. We use Equation (1) in Wu et al. (2010) to determine the line luminosity ($L_{\rm dense}$). The fraction of line tracer luminosity inside the region defined by the FWHM

Table 5
Line Fits

Source	Line	Intensity (K km s^{-1})	v (km s^{-1})	Δv (km s^{-1})	Rms (I) (K km s^{-1})	Note
G034.158+00.147	HCO^+	10.60	56.42 (0.02)	3.06 (0.05)	0.48	
G034.158+00.147	HCN	9.84	56.60 (0.03)	2.68 (0.05)	0.48	
G034.158+00.147	$H^{13}CO^+$	3.61	57.91 (0.09)	4.72 (0.22)	0.28	
G034.158+00.147	$H^{13}CN$	6.99	57.80 (0.11)	4.74 (0.25)	0.53	
G034.997+00.330	HCO^+	3.82	53.90 (0.03)	3.34 (0.09)	0.23	
G034.997+00.330	HCN	7.19	54.50 (0.02)	3.02 (0.05)	0.30	
G034.997+00.330	$H^{13}CO^+$	0.42	53.27 (0.14)	2.20 (0.35)	0.17	
G034.997+00.330	$H^{13}CN$	1.04	53.60 (0.17)	2.95 (0.39)	0.34	
G036.459−00.183	HCO^+	1.67	77.91 (0.06)	2.56 (0.15)	0.33	
G036.459−00.183	HCN	1.72	78.50 (0.11)	2.94 (0.25)	0.33	
G037.677+00.155	HCO^+	1.15	82.95 (0.07)	2.52 (0.10)	0.15	
G037.677+00.155	HCN	0.48	82.90 (0.21)	3.93 (0.56)	0.25	
G045.825−00.291	HCO^+	1.31	50.45 (0.22)	5.35 (0.56)	0.35	
G045.825−00.291	HCN	2.23	50.18 (0.41)	11.1 (0.98)	0.51	
G046.495−00.241	HCO^+	1.20	51.35 (0.08)	2.23 (0.20)	0.11	v1
G046.495−00.241	HCN	0.96	51.20 (0.14)	2.75 (0.40)	0.15	v1
G046.495−00.241	HCO^+	0.55	54.48 (0.14)	1.93 (0.34)	0.10	v2
G046.495−00.241	HCN	0.65	54.40 (0.16)	2.27 (0.57)	0.08	v2
G046.495−00.241	HCO^+	1.05	58.54 (0.15)	3.05 (0.45)	0.16	v3
G046.495−00.241	HCN	1.61	58.80 (0.19)	2.21 (0.36)	0.16	v3, hfs

Note. (1) v1 mean velocity component 1. (2) hfs mean fit to hyperfine components.

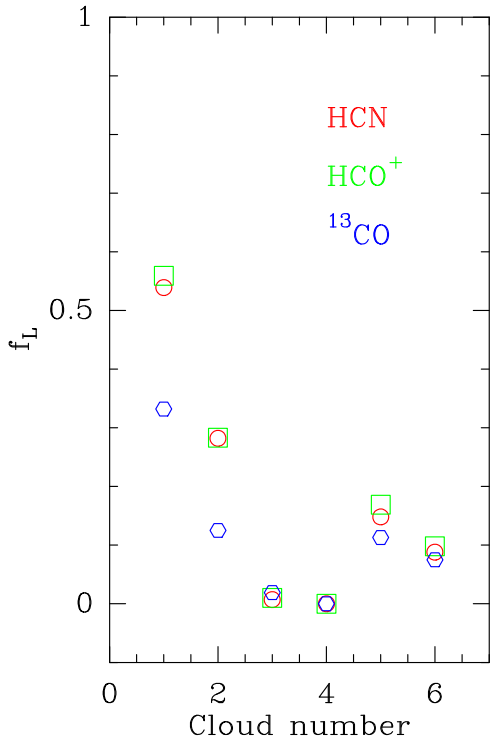

Figure 10. The fraction of luminosity (f_L) within the $A_V > 8$ mag region is plotted for each tracer vs. cloud number, in the order they appear in all of the tables. Different symbols and colors are used to separate the different tracers.

of the tracer, extended to a full Gaussian, was determined by dividing L_{dense} by the total luminosity in Table 3.

We use Equation (3) of Wu et al. (2010) to compute the dense gas mass from the virial theorem (M_{dv}). From M_{dv}, the surface density (Σ_{dense}) and volume-averaged density ($\bar{n}$) of the gas in the region defined by the line tracer are computed, using Equations (5) and (6) from Wu et al. (2010). The clump properties determined from HCN are shown in Table 6, while those determined from HCO^+ are shown in Table 7. The values in the tables have too many significant digits, but the errors given in the tables clarify how many are truly significant.

The distance uncertainties from Table 1 are propagated to other quantities. The virial mass is determined from the distance and linewidth; for the linewidth, the value and uncertainty from the line fits are propagated. These uncertainties also enter the uncertainties for the surface density (Σ) and average density ($\bar{n}$) of the clump. Even with possible underestimates for the uncertainties in angular size, the propagated uncertainty in the clump properties is substantial, especially for $\bar{n}$, which depends strongly on the size. Distance uncertainties were not included in ratios where the distance cancels out, such as M_{dense}/L_{dense}.

The means, standard deviations, and medians are given at the bottom of each table. The properties vary widely from cloud to cloud, as indicated by the very substantial standard deviations (larger or comparable to the mean values). In particular, G036.459−00.183 has a very large value of r_{dense} for HCO^+, reflecting the very diffuse emission in that tracer; the nominal fraction of the luminosity inside the Gaussian is greater than unity, while the surface and volume densities are very low. Clearly, HCO^+ is not tracing dense gas in this source; HCN indicates a smaller size and lower f_L, leading to larger surface and volume densities but is still more characteristic of clouds than of clumps.

For comparison, Wu et al. (2010) found a median r_{dense} of 0.71, a median M_{dense} of $2.7 \times 10^3\,M_\odot$, and the median $\bar{n}$ of 1.6×10^4 cm^{-3}. The regions probed by the half-power size of line tracer emission in the current sample are larger in size but similar in mass and, therefore, lower in both surface density and mean density. The sample of Wu et al. (2010) was derived from studies originally selected by the presence of water masers and, subsequently, strong emission from CS $J = 7 \rightarrow 6$, so

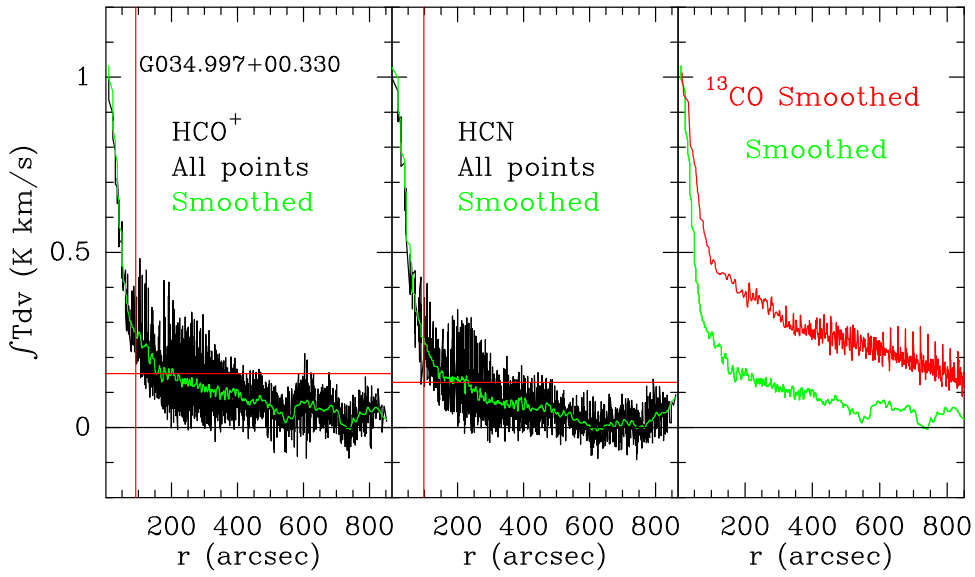

Figure 11. The integrated intensity of the HCO^+ and HCN lines as a function of distance from the peak position of each for G034.997+00.330. The red vertical line shows the FWHM size that defines the dense core. The red horizontal line is drawn at three times the rms noise in the normalized intensity. The panel on the right shows the HCO^+ and ^{13}CO lines together, after Hanning smoothing by 30 points.

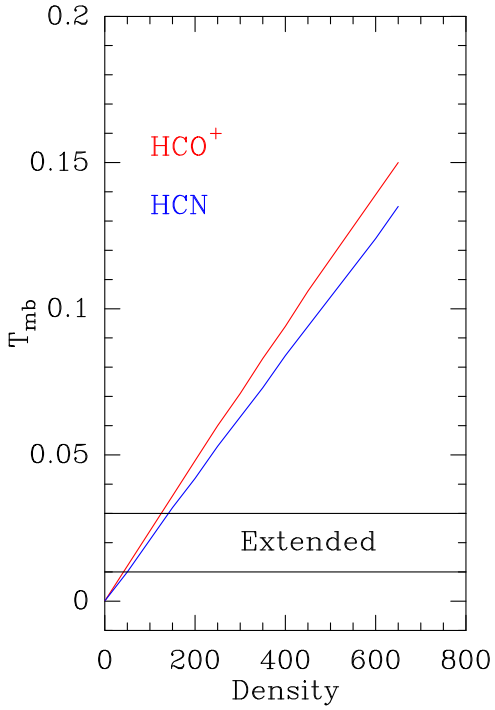

Figure 12. The main-beam temperature is plotted vs. the density of colliding particles, with HCO^+ in red and HCN in blue. Typical observations in the regions outside the $A_V > 8$ mag regions are shown as horizontal lines.

they probably represented particularly dense regions (Plume et al. 1997).

Comparing HCO^+ and HCN, the clump properties are broadly similar. Using the full width of the half-power size to define the dense clump produces similar results for the two tracers in the median, though differences can be seen in individual sources (e.g., G036.459−00.183). While chemical differences caused by factors like proximity to ionizing sources may well introduce differences between these two tracers in other sources, the two tracers produce similar results in this sample of Galactic sources.

5.2.3. Virial Parameters

Whether or not a particular region is primed to form stars depends most simply on the relative importance of turbulence versus gravity. This competition is crudely captured by the virial parameter. However, measuring the virial parameter is difficult, especially for substructures within clouds, for which boundaries are somewhat arbitrary and the contribution of the surrounding material is ignored (Mao et al. 2019). It is, however, something observers can estimate.

Table 8 presents the virial parameters, calculated from $\alpha_{dv} = M_{dv}/M_{dense}$. For G046.495−00.241, the values of M_{dv} for the three separate velocity components have been added together for comparison to M_{dense}, which includes all of the BGPS sources. For some clouds, the BGPS and dense line tracer maps agree well, but for others, the agreement is poor (see Figures 1–6). The calculation of α_{dv} for the latter group of clouds is, at best, a crude indicator.

The first two sources have small values for α_{dv}. The other four sources have $\alpha_{dv} \geqslant 1$, consistent within uncertainties with unbound structures and certainly less dominated by gravity. The spread in α_{dv} in this sample is consistent with the range of values found for BGPS sources in general by Svoboda et al. (2016), with the first two sources lying near the lowest 10% point of the distribution (Table 7 of Svoboda et al. 2016), but our median values are higher than those for the full BGPS sample.

6. Discussion

6.1. The Concept of a Dense Gas Tracer

The idea that certain molecules are tracers of dense gas has its origin in the early days of molecular line astronomy. At that time, sensitivities were poor, maps were small, and thus, the maps of dense gas line tracers were much smaller than those of CO and ^{13}CO. Studies of multiple transitions of molecules like CS and H_2CO provided evidence for gas with densities of about $n \sim 10^5\,cm^{-3}$ (Snell et al. 1984; Mundy et al. 1986, 1987). These studies and many others led to the naive

Table 6
Clump Properties for HCN

Source	$r_{\rm dense}$ (pc)	$L_{\rm dense}$ (K km s^{-1} pc^2)	$f_{\rm L}$	$M_{\rm dv}$ ($M_\odot$)	Σ ($M_\odot$ pc^{-2})	$\bar{n}$ (cm^{-3})	Note
G034.158+00.147	$0.86^{+0.16}_{-0.14}$	$94.1^{+36.2}_{-32.7}$	$0.20^{+0.07}_{-0.07}$	2845^{+596}_{-548}	1237^{+259}_{-238}	18538^{+7163}_{-6477}	
G034.997+00.330	$2.01^{+0.37}_{-0.37}$	$438.9^{+169.3}_{-169.8}$	$0.21^{+0.08}_{-0.08}$	1454^{+533}_{-533}	114^{+42}_{-42}	728^{+352}_{-352}	
G036.459−00.183	$3.61^{+0.39}_{-0.40}$	$246.4^{+71.2}_{-72.2}$	$0.28^{+0.08}_{-0.08}$	3535^{+563}_{-569}	86^{+14}_{-14}	306^{+75}_{-76}	
G037.677+00.155	$1.74^{+0.24}_{-0.24}$	$18.4^{+7.8}_{-7.8}$	$0.11^{+0.04}_{-0.04}$	1652^{+264}_{-264}	173^{+28}_{-28}	1274^{+367}_{-368}	
G045.825−00.291	$2.49^{+0.32}_{-0.34}$	$166.0^{+57.2}_{-59.6}$	$0.12^{+0.04}_{-0.04}$	10631^{+2605}_{-2658}	547^{+134}_{-137}	2816^{+928}_{-970}	
G046.495−00.241	$1.12^{+0.25}_{-0.23}$	$14.4^{+6.7}_{-6.3}$	$0.06^{+0.03}_{-0.03}$	830^{+235}_{-224}	211^{+60}_{-57}	2421^{+1148}_{-1069}	v1
G046.495−00.241	$1.02^{+0.23}_{-0.21}$	$8.3^{+3.9}_{-3.6}$	$0.04^{+0.02}_{-0.01}$	565^{+235}_{-230}	174^{+73}_{-71}	2199^{+1247}_{-1187}	v2
G046.495−00.241	$1.45^{+0.31}_{-0.28}$	$37.9^{+16.4}_{-15.1}$	$0.17^{+0.07}_{-0.06}$	2020^{+732}_{-711}	304^{+110}_{-107}	2678^{+1377}_{-1297}	v3
Mean	1.79	128.1	0.147	2942	356	3870	
Std. Dev.	0.86	141.7	0.075	3048	360	5611	
Median	1.60	66.0	0.144	1836	193	2310	

Note. v1, v2, etc. indicate the velocity component when separated.

Table 7
Clump Properties for HCO^+

Source	$r_{\rm dense}$ (pc)	$L_{\rm dense}$ (K km s^{-1} pc^2)	$f_{\rm L}$	$M_{\rm dv}$ ($M_\odot$)	Σ ($M_\odot$ pc^{-2})	$\bar{n}$ (cm^{-3})	Note
G034.158+00.147	$0.55^{+0.14}_{-0.13}$	$56.2^{+30.3}_{-28.9}$	$0.16^{+0.09}_{-0.08}$	1819^{+487}_{-463}	1936^{+518}_{-492}	45358^{+23133}_{-21888}	
G034.997+00.330	$1.82^{+0.36}_{-0.36}$	$205.7^{+89.0}_{-89.2}$	$0.17^{+0.07}_{-0.07}$	1316^{+494}_{-495}	126^{+47}_{-47}	889^{+454}_{-455}	
G036.459−00.183	$6.32^{+0.54}_{-0.56}$	$681.6^{+177.7}_{-180.9}$	$1.06^{+0.26}_{-0.28}$	6184^{+895}_{-908}	49^{+7}_{-7}	100^{+21}_{-21}	
G037.677+00.155	$2.52^{+0.24}_{-0.24}$	$81.7^{+18.7}_{-18.8}$	$0.66^{+0.15}_{-0.15}$	2389^{+293}_{-294}	120^{+15}_{-15}	609^{+124}_{-124}	
G045.825−00.291	$3.21^{+0.34}_{-0.37}$	$150.7^{+51.3}_{-53.5}$	$0.42^{+0.14}_{-0.14}$	13722^{+3213}_{-3286}	424^{+99}_{-101}	1690^{+501}_{-529}	
G046.495−00.241	$0.61^{+0.17}_{-0.16}$	$7.7^{+4.5}_{-4.3}$	$0.05^{+0.03}_{-0.03}$	456^{+151}_{-146}	385^{+127}_{-123}	8045^{+4704}_{-4495}	v1
G046.495−00.241	$1.15^{+0.25}_{-0.23}$	$8.6^{+4.1}_{-3.8}$	$0.05^{+0.02}_{-0.02}$	638^{+265}_{-259}	154^{+64}_{-62}	1722^{+966}_{-919}	v2
G046.495−00.241	$0.76^{+0.19}_{-0.18}$	$8.8^{+4.7}_{-4.5}$	$0.06^{+0.03}_{-0.03}$	1058^{+411}_{-400}	580^{+225}_{-220}	9762^{+5701}_{-5446}	v3
Mean	2.12	150.1	0.328	3448	472	8522	
Std. Dev.	1.82	211.9	0.341	4241	580	14333	
Median	1.48	69.0	0.167	1568	270	1706	

Note. v1, v2, etc. indicate the velocity component when separated.

Table 8
Virial Parameters

Source	$\alpha_{\rm dv}$(HCN)	$\alpha_{\rm dv}$(HCO^+)	Note
G034.158+00.147	$0.21^{+0.04}_{-0.03}$	$0.13^{+0.02}_{-0.02}$	
G034.997+00.330	$0.12^{+0.06}_{-0.06}$	$0.11^{+0.06}_{-0.06}$	
G036.459−00.183	$1.13^{+0.47}_{-0.47}$	$2.01^{+0.83}_{-0.82}$	
G037.677+00.155	$1.62^{+0.73}_{-0.72}$	$2.29^{+1.03}_{-1.01}$	
G045.825−00.291	$1.35^{+0.61}_{-0.61}$	$1.72^{+0.77}_{-0.78}$	
G046.495−00.241	$4.79^{+2.14}_{-2.11}$	$3.11^{+1.39}_{-1.37}$	1
Mean	1.54	1.56	
Std. Dev.	1.56	1.10	
Median	1.24	1.86	

Note. (1) Combination of the three velocity components.

idea that a single line of these molecules indicated the presence of gas of a certain density, often described as the critical density.

The idea of a critical density arose among radio astronomers when most observations were at centimeter wavelengths, for which the Rayleigh–Jeans limit is appropriate. In that limit, the excitation temperature of a line increases from the background temperature of about 2.73 K up the kinetic temperature over a wide range of densities (two to three orders of magnitude). By balancing spontaneous radiative decay and collisional de-excitation, a "critical" density can be defined. As discussed in detail by Evans (1989), the critical density in the R-J limit lies near the low-density limit of the wide range described above, just as the excitation temperature begins to rise above the background, but the critical density instead lies near the *high*-density end of the range, near thermalization, for millimeter-wave lines, where the R-J approximation is not valid. Consequently, for millimeter-wave lines, almost all emission arises from gas well below the critical density, commonly called sub-thermal emission. Thus, even for the simplified two-level molecule, the idea that a particular line arises in gas above the critical density of that line is incorrect.

Once one drops the two-level approximation, considers collisions to higher levels, and includes trapping, lines can be appreciably excited at even lower densities. To make this point, Evans (1999) introduced the concept of the effective density: the density needed to produce a line of $T_{\rm mb} = 1$ K. Shirley (2015)

explored these issues in greater detail and computed effective densities (now for the integrated intensity of 1 K km s^{-1}) for many transitions, confirming that many are orders of magnitude less than the corresponding critical densities. The largest discrepancies between effective and critical densities occur for the resonance transitions, $J = 1 \rightarrow 0$, which are the ones used in extragalactic studies and in this paper. For example, the effective density for $J = 1 \rightarrow 0$ is 9.5×10^2 cm^{-3} versus a critical density of 6.8×10^4 cm^{-3} for HCO$^+$; the values are 8.4×10^3 cm^{-3} versus 4.7×10^5 cm^{-3} for HCN.

To properly interpret maps of very large regions of clouds in our Galaxy and observations of other galaxies, it is important to ask, what is the effective density that can produce the distributed emission that we see, which is at a level much lower than the 1 K km s^{-1} criterion used by Shirley (2015)? As shown in Figure 12, for the $J = 1 \rightarrow 0$ lines of HCN and HCO$^+$, the entire molecular cloud, at densities of 50–100 cm^{-3} and column densities corresponding to $A_V \approx 1$, can produce the weak emission that we observe. We have considered only collisions with H_2 and He. Electron collisions may be important for low extinction regions of the cloud, further increasing the emission at low neutral densities (Goldsmith & Kauffmann 2017). Weak emission ($T_A^* = 0.02$–0.1 K) in the HCO$^+$ $J = 1 \rightarrow 0$ line from diffuse clouds ($n \approx 100$ cm^{-3}) was observed some time ago (Liszt & Lucas 1994). In most cases, the area of this weak emission is large enough that its weak emission dominates the regions of truly dense gas in determining the total luminosity of the line tracer.

We must now ask if there is any remaining validity to using dense gas tracers. The answer depends on the use we make of them. We cannot say that they "probe only the dense gas", but their emission does concentrate into the dense regions better than CO or ^{13}CO (see Figure 11). Also, lines like HCO$^+$ $J = 1 \rightarrow 0$, used in combination with other lines, like isotopologues of CO, can reveal different regimes of density (Bron et al. 2018). Star formation rates are predicted more consistently from nearby clouds to distant galaxies using the still loosely defined dense gas than from using CO (Vutisalchavakul et al. 2016). Lines from higher J levels will be more strongly biased toward denser gas, but they are harder to observe.

6.2. Comparison to Other Work

As the $J = 1 \rightarrow 0$ transition of HCN became more accepted as a probe of dense gas in the extragalactic community, a number of studies began to examine the origin of HCN (and other putative tracers of dense gas) in molecular clouds in the Galaxy. We compare our results to those of other studies in this section.

Pety et al. (2017) mapped a number of molecular lines in Orion B. They found small fractions of the luminosity of HCN (18%) and HCO$^+$ (16%) coming from regions with $A_V > 15$ mag. They stated that, "the common assumption that lines of large critical densities ($\approx 10^5$ cm^{-3}) can only be excited by gas of similar density is clearly incorrect." Instead, they conclude that HCN and HCO$^+$ mostly trace densities from 500 to 1500 cm^{-3}. They note that the tracer that is most strongly concentrated in the densest gas is N_2H^+, because of chemistry.

Kauffmann et al. (2017) mapped HCN $J = 1 \rightarrow 0$ toward Orion A. They found that it mainly traced gas with $A_V \approx 6$ mag or $n \approx 870$ cm^{-3}. They agreed that N_2H^+ was the best tracer of truly dense gas. They also limited the conversion factor, $M_{dense} \leqslant 20L$(HCN), the same as our average value.

Shimajiri et al. (2017) mapped the $J = 1 \rightarrow 0$ transitions of HCN, HCO$^+$, and their rarer isotoplogues in the nearby clouds, Aquila, Ophiuchus, and Orion B. They found that the HCN and HCO$^+$ lines traced the gas down to $A_V \approx 2$ or $n \approx 1 \times 10^3$ cm^{-3}. They found that the conversion factors (α_{tot}) are anticorrelated with the local FUV field strength. Nguyen-Luong et al. (2020) studied HCN and HCO$^+$ $J = 1 \rightarrow 0$ toward the M17 cloud. They found that both lines traced equally well regions with column density above 3×10^{22} cm^{-2}, but a significant fraction of the total emission from the cloud came from regions below that column density, with substantial differences in regions of the cloud with different star formation histories. A. Barnes (2020, in preparation) studied the emission from a number of lines toward a distant ($d = 11.11$ kpc), massive (10^4–10^5 $M_\odot$) cloud, with similar results. While HCN $J = 1 \rightarrow 0$ emission is strongly enhanced in warm gas at high column densities, a substantial fraction arises in lower column density gas.

Our results are broadly consistent with these works and extend their conclusions into the inner Galaxy. By considering the far outer regions of clouds without detections at individual positions, we show that even lower intensity levels may dominate the total luminosity of a cloud in these lines. Simple calculations reveal that even at densities of about 100 cm^{-3}, emission, albeit at very low intensities, can rival or even dominate the more intense emission from the truly dense regions in determining the total luminosity of dense line tracers.

7. Conclusions

The main conclusions can be summarized as follows.

1. The correlation between different tracers of dense gas (extinction, millimeter-wave continuum emission, HCN, HCO$^+$) varies from cloud to cloud.
2. Broadly, the clouds divide into two groups: one for which the dense line tracers are strong and concentrated, and the other for which they are weak and distributed.
3. In clouds where the dense line tracers are sharply peaked, all of the tracers show a general agreement and are more concentrated than the ^{13}CO emission.
4. In clouds with only weak, distributed emission from dense line tracers, the agreement is poor, and ^{13}CO traces similar material.
5. Even when the agreement is good, a substantial fraction of the line luminosity arises outside the dust-based measures of dense gas.
6. The agreement of dense line tracers with millimeter-wave continuum emission is better than the agreement for $A_V > 8$ mag. At the distances of some of these clouds, the millimeter-wave continuum emission from BGPS is typically tracing lower-density gas.
7. Measurements of L(HCN) toward other galaxies will likely include a large fraction of emission from relatively low-density gas, unless the other galaxy is a starburst galaxy. This variation may be responsible for some of the observed scatter between galaxies in the study of Jiménez-Donaire et al. (2019).
8. The conversion from luminosity to mass of dense gas, as measured by extinction or millimeter-wave continuum emission, is quite variable. For the dense regions, the

conversion factor is about 20, while it is closer to 6 if the line luminosity of the whole cloud is included.

9. For this sample, HCN and HCO^+ seem to probe about the same material. They are equally good (or bad) tracers.
10. The regions probed in this paper in HCN and HCO^+ in two clouds in the sample are similar to those originally studied by Wu et al. (2010) but are somewhat larger and less dense. The regions probed in the other clouds are substantially more diffuse and less clearly bound.
11. The distributed emission of HCN and HCO^+ can arise from regions of very low density, $n = 50$–$100\,cm^{-3}$. Because of the large area of most clouds at such low densities, these less dense regions can dominate the total luminosity of line tracers.

We thank the staff of the TRAO for support during the course of these observations. N.J.E. thanks the Department of Astronomy at the University of Texas at Austin for ongoing research support. J.W. is supported by NSFC grant Nos. 11590783 and 11673029 and National Key R&D Program of China No. 2017YFA0402600.

Appendix

In each section, we discuss the details for each cloud. The data reduction details are contained in Table B1.

Appendix A
G034.158+00.147

Our map was centered, not on the source name position, but on $l = 34.250$, $b = 0.150$, near the H II region, G34.26+0.15. This cloud has been studied extensively under other names. The clumps to the "northeast" in our maps are associated with the IRDC 34.43+0.24, in which Rathborne et al. (2006) identified 9 mm continuum sources. These are blended into two clumps in the HCN/HCO^+ maps. G34.26−0.15 is a well-known star-forming region with a water maser (Hofner & Churchwell 1996) and a methanol maser (Breen et al. 2015; Kim et al. 2019).

The near kinematic distance is 3.7 kpc (Anderson et al. 2014). A VERA parallax measurement (Kurayama et al. 2011) of a water maser found by Wang et al. (2006) gives the distance as $1.56^{+0.12}_{-0.11}$ kpc, but Kurayama et al. (2011) note that the cloud would then have a peculiar velocity of about 40 $km\,s^{-1}$. Because this seems unlikely, we follow other recent work in using the kinematic distance. IRDC G034.43+00.24 has a polarization map (Soam et al. 2019).

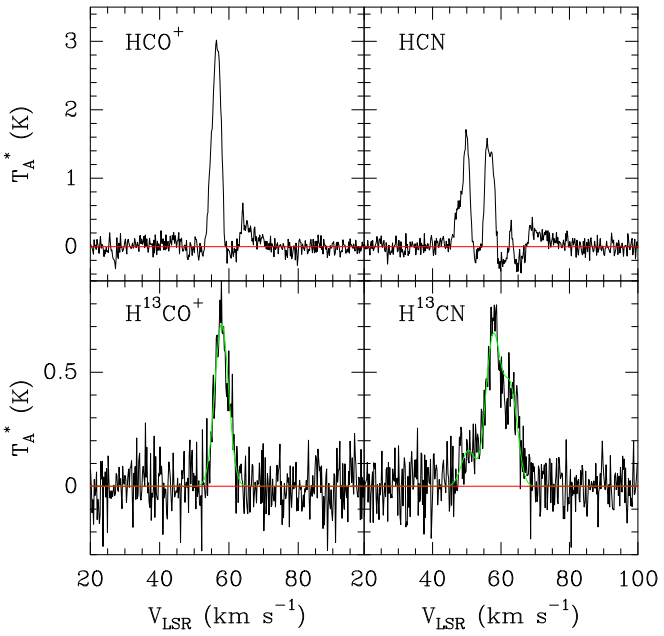

Figure A1. The spectra of HCO^+, HCN, $H^{13}CO^+$, and $H^{13}CN$ toward the peak of G034.158+00.147. In each plot, the red line shows the zero level. For the rare isotopologues, the green line shows the fit to the line.

The BGPS millimeter continuum emission is shown in Figure 1. The maps of integrated intensity peak about 25″ east (higher l) of the reference position, essentially on top of the H II region. Both HCN and HCO^+ show self-absorption and even absorption below zero around 60 $km\,s^{-1}$, while the $H^{13}CO^+$ spectrum shows a clear peak at somewhat higher velocities than those of the main lines (Figure A1). The isotopologues peak slightly north of the main lines. The HCN line is particularly badly affected by absorption. We attribute this effect to the actual absorption of the continuum from the H II region, which has been subtracted out by baseline process. Similar continuum absorption has been seen in HCO^+ $J = 1 \rightarrow 0$ and HCN

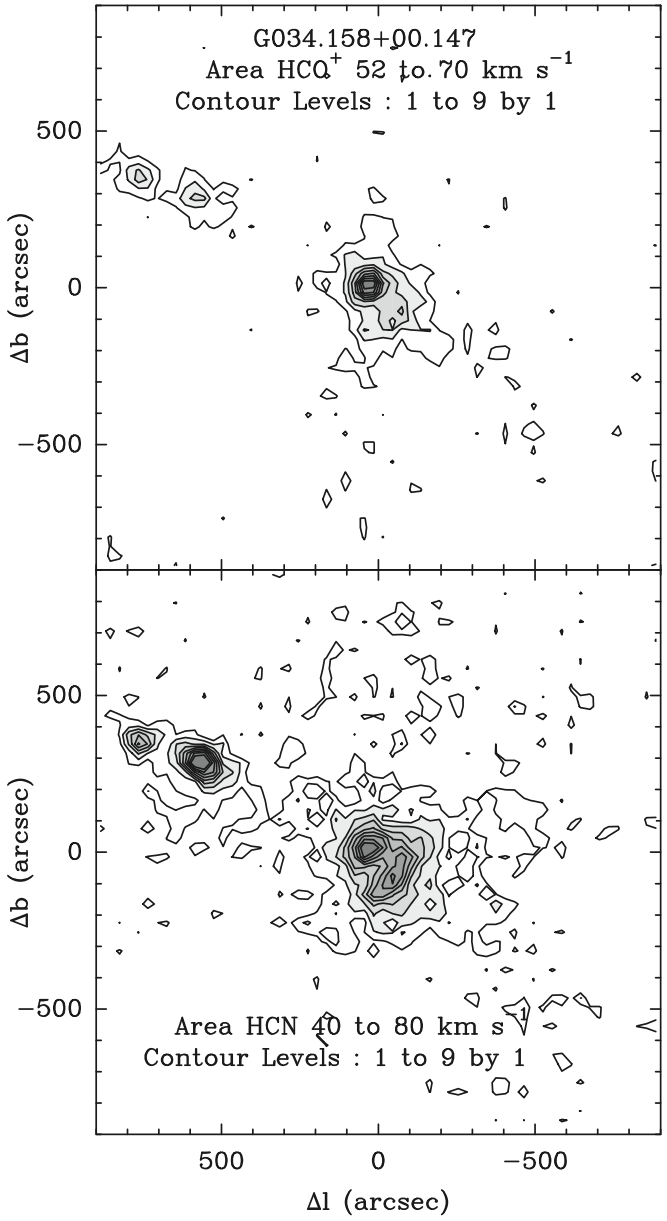

Figure A2. The integrated intensities of the HCO^+ (top panel) and HCN (bottom panel) lines in G034.158+00.147. The integration is over the range of 52–70 km s^{-1} for HCO^+ and 40–80 km s^{-1} for HCN.

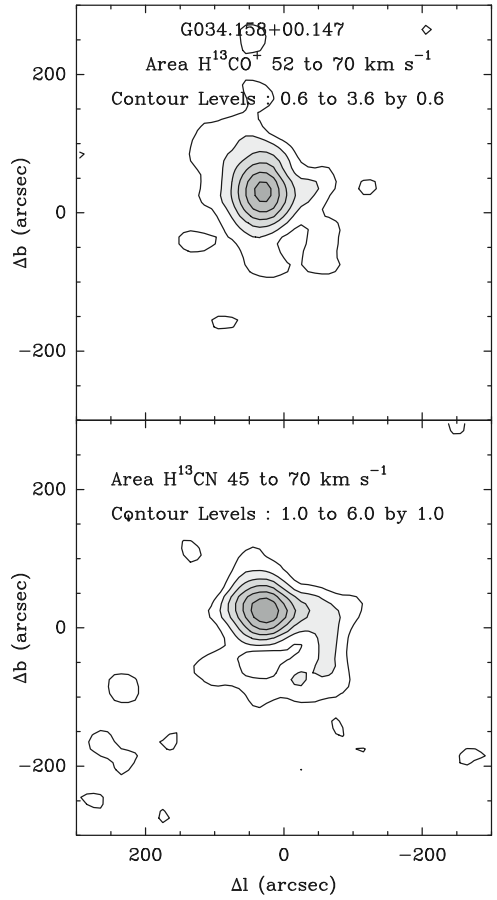

Figure A3. The integrated intensities of the $H^{13}CO^+$ (top panel) and $H^{13}CN$ (bottom panel) lines in G034.158+00.147. The integration is over the range of 52–70 km s^{-1} for $H^{13}CO^+$ and 40–80 km s^{-1} for $H^{13}CN$.

$J = 3 \rightarrow 2$ by Liu et al. (2013), who interpret the line profiles as a signature of infall at about 3 km s^{-1}. Mookerjea et al. (2007) measured a continuum of 6.7 Jy at 2.8 mm in a source size of 1.″6 by 1.″4. This would produce a continuum temperature in our 58″ beam of $3.5(2.8/3.4)^a$ K, where a is the spectral index between the two wavelengths. Because both free–free and dust continuum emission are contributing in this spectral region, the value of a is uncertain, but the wavelengths are close enough that it makes little difference. There is clearly sufficient continuum emission to explain the absorption that we observe. For extragalactic observations, these issues would not be recognized. The contour diagrams for the main isotopologues are shown in Figure A2, and those for the rarer isotopologues are shown in Figure A3.

To determine core properties, we used the peak integrated intensity from the fit to the emission and linewidths from fits to the isotopic lines. For the HCN line properties (Table 5), we used the area within the window of 43–70 km s^{-1}, because the hyperfine components, the velocity structure, and the absorption made fits impossible. The $H^{13}CN$ line for peak 1 was fitted with hyperfine components.

Appendix B
G034.997+00.330

This cloud was mapped in equatorial coordinates with center position $\alpha_{2000} = 18^h54^m01^s.83$, $\delta_{2000} = 01°59'18''.0$. The BGPS millimeter continuum emission is shown in Figure 2. The spectra at the peaks indicated in Table B1 are shown in Figure B1. There is a single velocity component at about 57 km s^{-1}. The HCN line is well fitted with hyperfine components. The $H^{13}CO^+$ and $H^{13}CN$ lines are about 10% of the main lines, indicating only a modest optical depth. Nonetheless, we use the $H^{13}CO^+$ line averaged over its detected region for the linewidth in computing virial mass, etc.

The contour diagrams of the integrated intensity are shown in Figure B2. The BGPS, HCN, and HCO^+ emission regions correspond well. However, there is significant emission at large distances from the peak of the emission. The plots of the integrated intensity of HCO^+ and HCN versus distance from the peak are shown in Figure 11. The right-most panel shows the smoothed HCO^+ along with that from ^{13}CO.

Table B1
Reduction Details

Source	Line	v_{sp} (km s^{-1})	v_{win} (km s^{-1})	v_I (km s^{-1})	Peak Offset (arcsec)	Range (arcsec)	Notes
G034.158+00.147	HCO^+	20, 100	52, 70	52, 70	27, 10	−200, 160; −220, 140	
G034.158+00.147	HCN	20, 100	40, 80	40, 80	20, 4	−300, 280; −280, 240	
G034.158+00.147	$H^{13}CO^+$	20, 100	52, 70	52, 70	31, 29	−80, 120; −80, 140	
G034.158+00.147	$H^{13}CN$	20, 100	40, 80	45, 70	27, 20	−80, 100; −80, 100	
G034.997+00.330	HCO^+	20, 80	40, 65	40, 65	−20, 110	−220, 140; −160, 220	
G034.997+00.330	HCN	20, 80	42, 63	42, 60	−20, 110	−220, 140; −160, 220	
G034.997+00.330	$H^{13}CO^+$	20, 80	45, 60	45, 60	−20, 110	−80, 20; 80, 160	
G034.997+00.330	$H^{13}CN$	20, 80	42, 63	42, 63	−20, 110	−80, 20; 80, 160	
G036.459−00.183	HCO^+	20, 120	45, 85	68, 95	−61, −32	−160, 80; −200, 380	
G036.459−00.183	HCN	20, 120	43, 93	67, 93	−20, −20	−100, 180; −160, 340	
G037.677+00.155	HCO^+	20, 120	40, 50; 75, 90	77, 88	−98, −156	−180, 120; −240, 0	
G037.677+00.155	HCN	20, 120	40, 50; 73, 93	73, 93	−40, −120	−160, 240; −700, 20	
G045.825−00.291	HCO^+	20, 80	45, 65	45, 65	−418, 60	−500, −180; 20, 180	
G045.825−00.291	HCN	20, 80	45, 65	40, 65	−400, 80	−480, −220; −20, 220	
G046.495−00.241	HCO^+	20, 100	40,70	47, 53	87, 3	−20, 120; −60, 200	1
G046.495−00.241	HCN	20, 100	40,70	47, 53	83, 13	−60, 140; −40, 80	1
G046.495−00.241	HCO^+	20, 100	40,70	53, 56	−63, 74	−140, 340; 0, 120	2
G046.495−00.241	HCN	20, 100	40,70	53, 56	276, 150	−140, 340; −60, 200	2
G046.495−00.241	HCO^+	20, 100	40,70	56, 60	−307,104	−540, −140; −20, 200	3
G046.495−00.241	HCN	20, 100	40,70	56, 65	−292,109	−540, 300; −60, 200	3

Note. (1) Position of center peak, velocity component v1. (2) Position of eastern peak, velocity component v2. (3) Position of western peak.

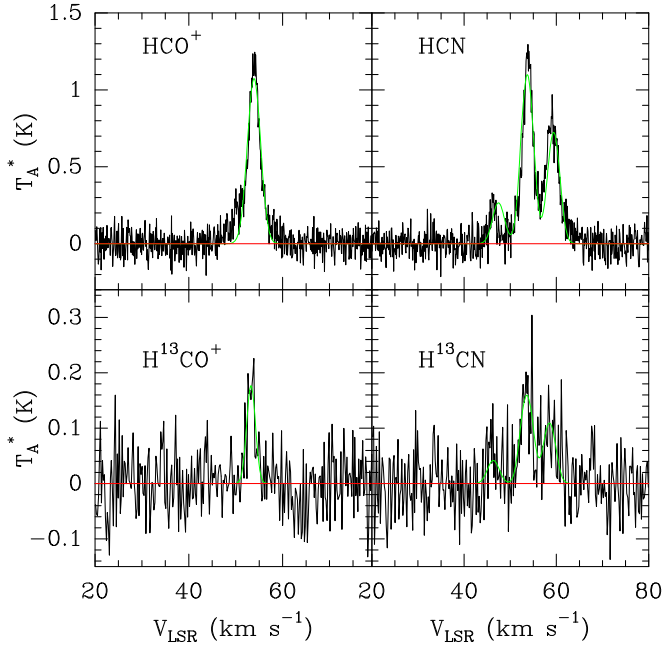

Figure B1. Top panels: the spectra of the HCO^+ and HCN lines at (−20, 100) for source G034.997+00.330. The HCN shows a fit to hyperfine structure. Bottom panels: the spectrum of the $H^{13}CO^+$ and $H^{13}CN$ lines averaged over the nine positions around (−20, 100). The $H^{13}CN$ line was fitted with hyperfine structure. In each plot, the red line shows the zero level, and the green line shows the fit.

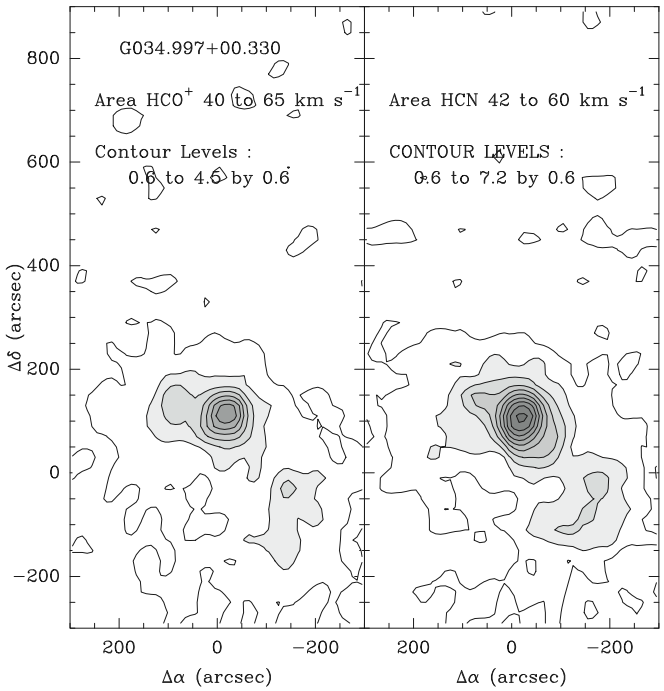

Figure B2. The integrated intensities of the HCO^+ and HCN lines in G034.997 +00.330. The integration is over the range of 45–60 kms for HCO^+ and 43–65 km s^{-1} for HCN.

Appendix C
G036.459−00.183

This cloud was mapped in equatorial coordinates with center position $\alpha_{2000} = 18^h58^m31\overset{s}{.}78$, $\delta_{2000} = 03°03'18\overset{''}{.}2$. The BGPS millimeter continuum emission is shown in Figure 3. The spectra are shown in Figure C1. Neither the $H^{13}CO^+$ nor the $H^{13}CN$ lines was detected at any position. This cloud has a primary component at about 73 km s^{-1}, which is associated with the H II region, based on the recombination line velocity. A secondary component at about 55 km s^{-1} appears in the spectrum, but it is not related to this cloud, so we do not analyze it. The two components nearly overlap but are separable at about 67–68 km s^{-1}. Hyperfine structure was used to fit the HCN lines, but the integrated intensity was integrated over all hyperfine components.

The maps of HCO^+ and HCN are shown in Figure C2. The HCO^+ and HCN integrated intensity generally map similarly, though there are clearly differences in detail. The emission is not well peaked, and the half-power contour is nearly as large as the region of the detected emission, so the properties are poorly defined.

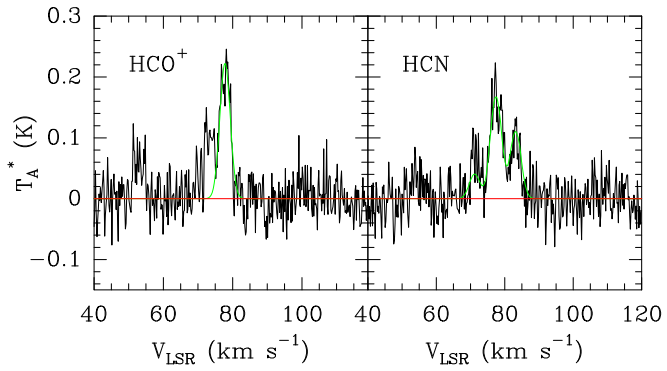

Figure C1. The spectra of HCO^+ and HCN toward the peak of G036.459 −00.183. In each plot, the red line shows the zero level, and the green line shows the fit to the line.

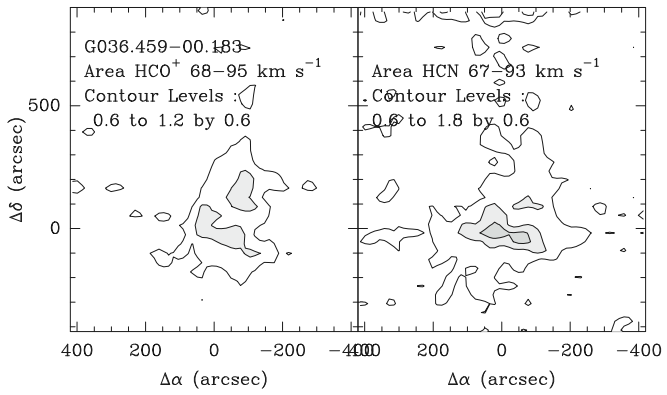

Figure C2. The integrated intensities of the HCO^+ and HCN lines for the 78 km s^{-1} component in G036.459−00.183.

Appendix D
G037.677+00.155

This source was mapped in galactic coordinates centered on the source name position, $l = 37.677$, $b = 0.155$. The BGPS millimeter continuum emission is shown in Figure 4. There are at least two velocity components: one near 45 km s^{-1} and one near 83 km s^{-1}. The second one is near the velocity of the radio recombination line for this H II region, so we focus on that. Figure D1 shows the spectra. Nine positions around a nominal

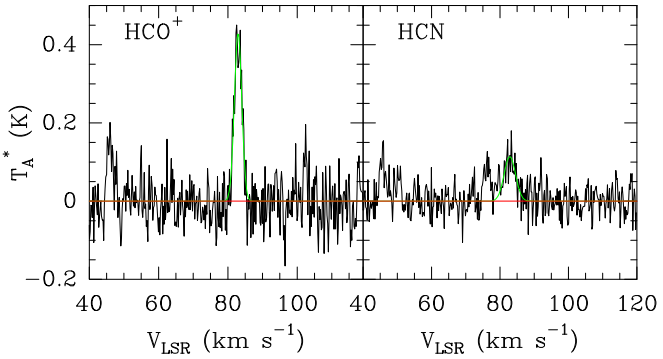

Figure D1. The spectra of HCO^+ and HCN toward their peaks in G037.677 +00.155. The HCO^+ line is at position (−100, −160); the HCN line is an average of the nine positions surrounding the offset (−40, −120). The HCN line was not well fitted with hyperfine structure, so only the main peak was fitted. Note that the peak positions are somewhat different for the two species. In each plot, the red line shows the zero level, and the green line shows the fit to the line.

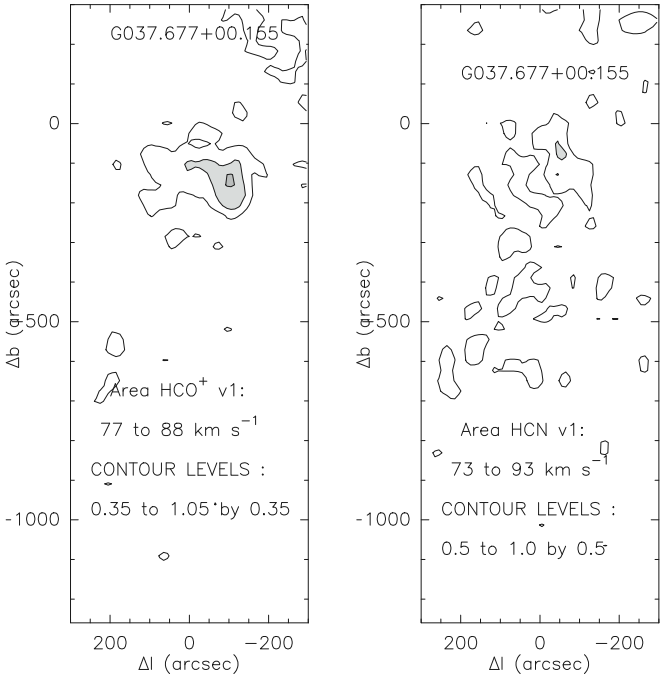

Figure D2. The integrated intensities of the HCO^+ and HCN lines in G037.677 +00.155 are shown for the velocity component near 82 km s^{-1}.

peak were averaged for HCN to produce the spectrum. The data were not well fitted with hyperfine structure, so we isolated the velocities around 83 km s^{-1} to be fitted.

The HCO$^+$ and HCN integrated intensity maps (Figure D2) show extended weak emission, so the peaks are not well defined. The peaks of the two lines differ. The weak emission is surprising because the cloud is relatively massive and has a substantial star formation rate and mass of dense gas, based on the submillimeter continuum data. However, the cloud was difficult to define, as it exists in a region of considerable line uncertainty in ^{13}CO.

Appendix E
G045.825−00.291

This source was mapped in galactic coordinates centered on the source name position, $l = 45.825$, $b = -0.291$. The BGPS millimeter continuum emission is shown in Figure 5. There are several peaks in the BGPS data. Only the "northwest" peak shows up in the HCO$^+$/HCN maps (Figure E2).

This source has two velocity components that are barely separable in HCO$^+$ and difficult to separate in HCN. Both of the HCO$^+$ and HCN lines are weak, but HCN is a bit stronger in integrated intensity. Figure E1 shows the spectra. We average over the nine positions around the peak to improve the noise since the lines are very similar. Since both velocity features peak in the same area, we include both in the maps of intensity. The isotopologue lines were not detected and did not provide useful constraints on optical depth. We plot the contours of emission for both main species (Figure E2); the peaks are slightly different for the two species but generally consistent. For HCO$^+$ and HCN, we use the velocity width and area of the 50.5 km s^{-1} feature to compute virial mass, etc. However, the HCN is made uncertain by hyperfine structure.

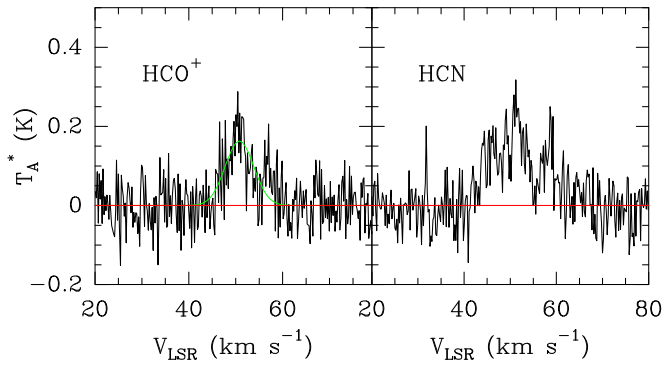

Figure E1. The spectra of HCO$^+$ and HCN toward their peaks in G045.825 −00.291. The HCO$^+$ line is an average of the nine positions surrounding the offset (−420, 60); the HCN line is an average of the nine positions surrounding the offset (−400, 80). The HCN line was not well fitted with hyperfine structure. Note that the peak positions are somewhat different for the two species. In each plot, the red line shows the zero level, and the green line shows the fit to the line.

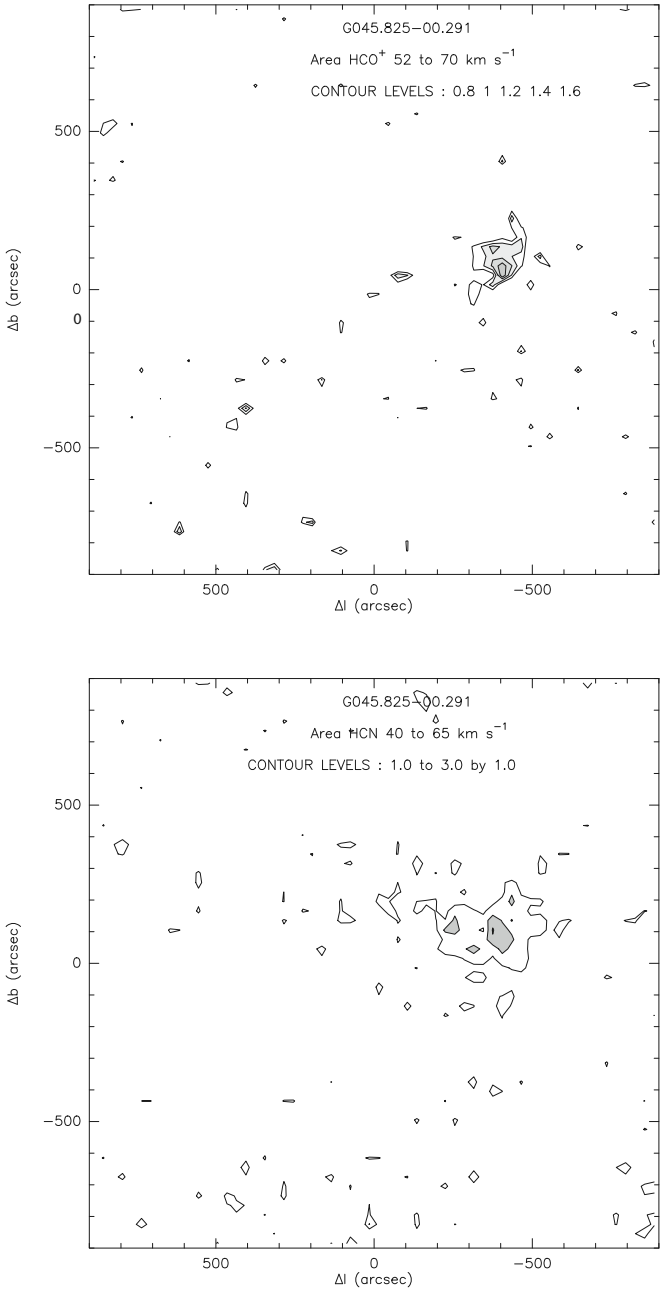

Figure E2. The integrated intensities of the HCO$^+$ and HCN lines for both components in G045.825−00.291 are shown.

Appendix F
G046.495−00.241

This source was mapped in galactic coordinates centered, not on the source name, but on $l = 46.400$, $b = -0.241$, because the source name was that of a millimeter-wave continuum source in the eastern part of the cloud. The BGPS millimeter continuum emission is shown in Figure 6. There are three regions of continuum emission, which we refer to as west,

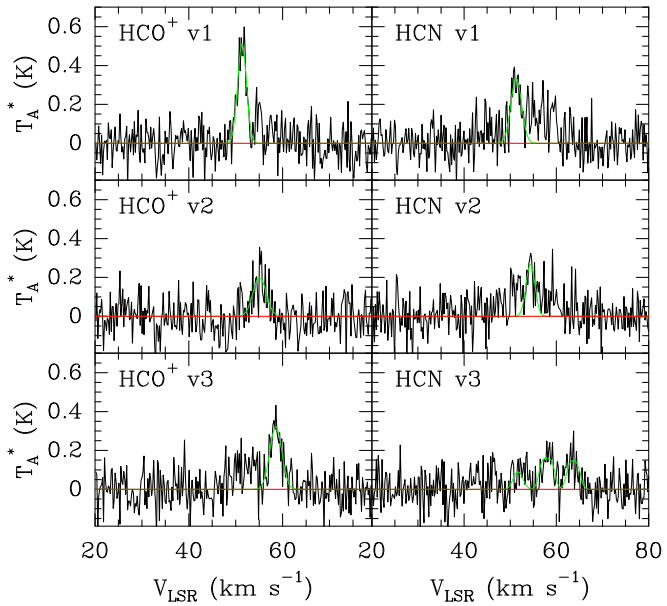

Figure F1. The spectra of HCO^+ and HCN toward the peaks for each velocity component in G046.495−00.241. The positions are those nearest the peak positions listed in Table B1. The HCN lines for the first two velocity components were not well fitted with hyperfine structure, so a single Gaussian was fitted to the main peak. In each plot, the red line shows the zero level, and the green line shows the fit to the line.

central, and east, in order of increasing longitude. Both HCO^+ and HCN appear to have several velocity components (Figure F1) and three separated emission regions when the emission is integrated over all velocities, which correspond roughly to the continuum peaks. There were no detections of the ^{13}C isotopologues, so we concluded that the velocity structure was unlikely to be caused by self-absorption.

It was possible to separate the three velocity components in HCO^+ and to make contour maps. The maps of the integrated intensity are shown in Figure F2. The spectra at the peaks of each component are shown in Figure F1. The lowest velocity component, v1, peaks most strongly on the central peak but has secondary peaks to the north and west that do not correspond exactly to the peaks of the other components but overlap with them. The middle velocity component (v2) emits over an extended region, but weakly, with no strong peaks. We picked the most central and largest peak, which is southeast of the peak of v1. The highest velocity component, denoted v3, peaks most strongly on the western (lower l) peak but has secondary maxima near the other peaks. The other lines are largely absent from the western peak. Because the individual velocity components are narrow, the rms in the integrated intensity is small, so it is possible to draw more contours. The secondary peaks and extended plateaus are reflected in the secondary maxima, but the main peak is reasonably well defined. The separation for HCN is more difficult because of hyperfine structure, so we used the velocity intervals from the HCO^+ analysis for components v1 and v2. Hyperfine structure was more visible and separate for v3, so we fit that component. The

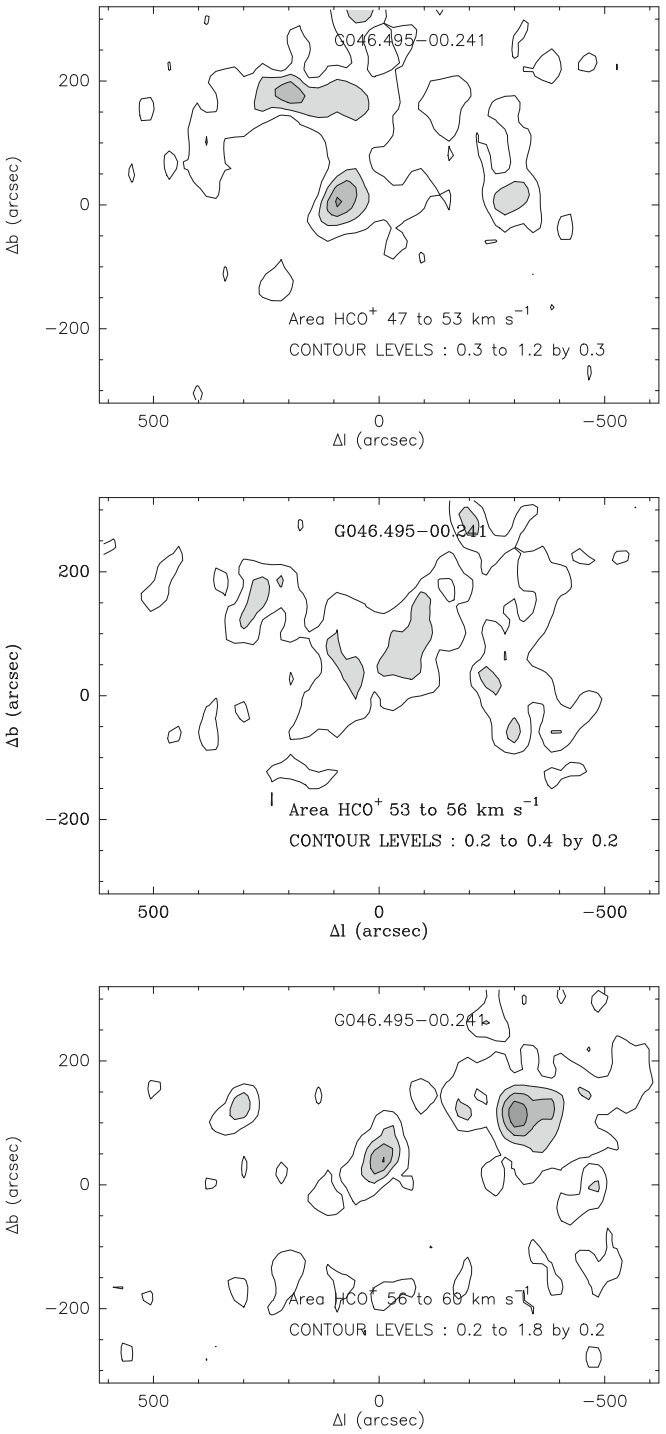

Figure F2. The integrated intensities of the HCO^+ lines in G046.495−00.241 are shown for the three different velocity components.

separation into velocity components would not be possible in the observations of other galaxies. The contour maps for each species and component in Figure F3 indicate the complexity of overlapping regions.

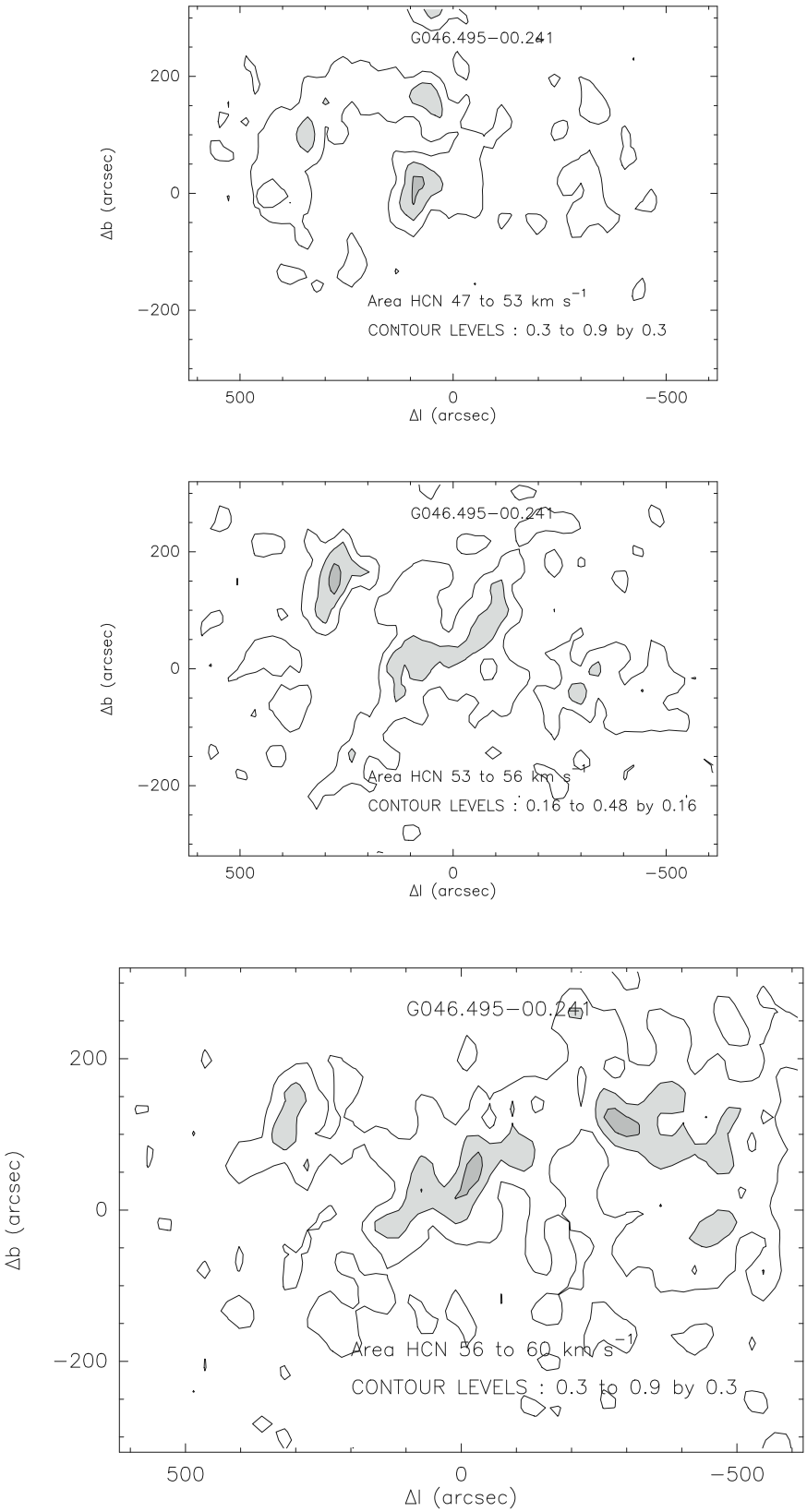

Figure F3. The integrated intensities of the HCN lines in G046.495−00.241 are shown for the three different velocity components.

ORCID iDs

Neal J. Evans, II https://orcid.org/0000-0001-5175-1777
Kee-Tae Kim https://orcid.org/0000-0003-2412-7092
Jingwen Wu https://orcid.org/0000-0001-7808-3756
Tie Liu https://orcid.org/0000-0002-5286-2564

References

Aguirre, J. E., Ginsburg, A. G., Dunham, M. K., et al. 2011, ApJS, 192, 4
Anderson, L. D., Bania, T. M., Balser, D. S., et al. 2014, ApJS, 212, 1
Barnes, P. J., Hernandez, A. K., O'Dougherty, S. N., Schap, W. J., III, & Muller, E. 2016, ApJ, 831, 67
Barnes, P. J., Yonekura, Y., Fukui, Y., et al. 2011, ApJS, 196, 12
Breen, S. L., Fuller, G. A., Caswell, J. L., et al. 2015, MNRAS, 450, 4109
Bron, E., Daudon, C., Pety, J., et al. 2018, A&A, 610, A12
DeLucia, F., & Gordy, W. 1969, PhRv, 187, 58
Dobbs, C. L., Burkert, A., & Pringle, J. E. 2011, MNRAS, 413, 2935
Dunham, M. K., Rosolowsky, E., Evans, N. J., II, Cyganowski, C., & Urquhart, J. S. 2011, ApJ, 741, 110
Evans, N. J., II 1989, RMxAA, 18, 21
Evans, N. J., II 1999, ARA&A, 37, 311
Evans, N. J., II, Heiderman, A., & Vutisalchavakul, N. 2014, ApJ, 782, 114
Gao, Y., & Solomon, P. M. 2004, ApJ, 606, 271
Ginsburg, A., Glenn, J., Rosolowsky, E., et al. 2013, ApJS, 208, 14
Goldsmith, P. F., & Kauffmann, J. 2017, ApJ, 841, 25
Heiderman, A., Evans, N. J., II, Allen, L. E., Huard, T., & Heyer, M. 2010, ApJ, 723, 1019
Helfer, T. T., & Blitz, L. 1997, ApJ, 478, 233
Hofner, P., & Churchwell, E. 1996, A&AS, 120, 283
Jackson, J. M., Rathborne, J. M., Shah, R. Y., et al. 2006, ApJS, 163, 145
Jeong, G.-I., Kang, H., Jung, J., et al. 2019, JKAS, 52, 227
Jiménez-Donaire, M. J., Bigiel, F., Leroy, A. K., et al. 2019, ApJ, 880, 127
Jones, P. A., Burton, M. G., Cunningham, M. R., et al. 2012, MNRAS, 419, 2961
Kauffmann, J., Goldsmith, P. F., Melnick, G., et al. 2017, A&A, 605, L5
Kim, W.-J., Kim, K.-T., & Kim, K.-T. 2019, ApJS, 244, 2
Kruijssen, J. M. D., Schruba, A., Hygate, A. P. S., et al. 2018, MNRAS, 479, 1866
Kurayama, T., Nakagawa, A., Sawada-Satoh, S., et al. 2011, PASJ, 63, 513
Lacy, J. H., Sneden, C., Kim, H., & Jaffe, D. T. 2017, ApJ, 838, 66
Lada, C. J., Forbrich, J., Lombardi, M., & Alves, J. F. 2012, ApJ, 745, 190
Lada, C. J., Lombardi, M., & Alves, J. F. 2010, ApJ, 724, 687
Liszt, H. S., & Lucas, R. 1994, ApJL, 431, L131
Liszt, H. S., & Pety, J. 2016, ApJ, 823, 124
Liu, L., Gao, Y., & Greve, T. R. 2015, ApJ, 805, 31
Liu, T., Wu, Y., & Zhang, H. 2013, ApJ, 776, 29
Mao, S. A., Ostriker, E. C., & Kim, C.-G. 2019, arXiv:1911.05078
Marsh, K. A., Whitworth, A. P., Lomax, O., et al. 2017, MNRAS, 471, 2730
McKee, C. F., & Tan, J. C. 2003, ApJ, 585, 850
Milam, S. N., Savage, C., Brewster, M. A., Ziurys, L. M., & Wyckoff, S. 2005, ApJ, 634, 1126
Mookerjea, B., Casper, E., Mundy, L. G., & Looney, L. W. 2007, ApJ, 659, 447
Mundy, L. G., Evans, N. J., II, Snell, R. L., & Goldsmith, P. F. 1987, ApJ, 318, 392
Mundy, L. G., Snell, R. L., Evans, N. J., II, Goldsmith, P. F., & Bally, J. 1986, ApJ, 306, 670
Nguyen-Luong, Q., Nakamura, F., Sugitani, K., et al. 2020, ApJ, 891, 66
Nguyen-Luong, Q., Nguyen, H. V. V, Motte, F., et al. 2016, ApJ, 833, 23
Pety, J., Guzmán, V. V., Orkisz, J. H., et al. 2017, A&A, 599, A98
Plume, R., Jaffe, D. T., Evans, N. J., II, Martín-Pintado, J., & Gómez-González, J. 1997, ApJ, 476, 730
Privon, G. C., Herrero-Illana, R., Evans, A. S., et al. 2015, ApJ, 814, 39
Rathborne, J. M., Jackson, J. M., & Simon, R. 2006, ApJ, 641, 389
Ripple, F., Heyer, M. H., Gutermuth, R., Snell, R. L., & Brunt, C. M. 2013, MNRAS, 431, 1296
Roh, D.-G., & Jung, J. H. 1999, PKAS, 14, 123
Sanders, D. B., Clemens, D. P., Scoville, N. Z., & Solomon, P. M. 1986, ApJS, 60, 1
Sastry, K. V. L. N., Herbst, E., & De Lucia, F. C. 1981, JChPh, 75, 4169
Shimajiri, Y., André, P., Braine, J., et al. 2017, A&A, 604, A74
Shirley, Y. L. 2015, PASP, 127, 299
Snell, R. L., Mundy, L. G., Goldsmith, P. F., Evans, N. J., II, & Erickson, N. R. 1984, ApJ, 276, 625
Soam, A., Liu, T., Andersson, B. G., et al. 2019, ApJ, 883, 95
Stephens, I. W., Jackson, J. M., Whitaker, J. S., et al. 2016, ApJ, 824, 29
Svoboda, B. E., Shirley, Y. L., Battersby, C., et al. 2016, ApJ, 822, 59
van der Tak, F. F. S., Black, J. H., Schöier, F. L., Jansen, D. J., & van Dishoeck, E. F. 2007, A&A, 468, 627
Vutisalchavakul, N., Evans, N. J., II, & Heyer, M. 2016, ApJ, 831, 73
Wang, Y., Zhang, Q., Rathborne, J. M., Jackson, J., & Wu, Y. 2006, ApJL, 651, L125
Wenger, T. V., Balser, D. S., Anderson, L. D., & Bania, T. M. 2018, ApJ, 856, 52
Wu, J., Evans, N. J., II, Gao, Y., et al. 2005, ApJL, 635, L173
Wu, J., Evans, N. J., II, Shirley, Y. L., & Knez, C. 2010, ApJS, 188, 313